A MODULAR SPECT CAMERA COMBINING PMTS AND SIPMS

by

Kimberly Jolene Doty

A Dissertation Submitted to the Faculty of the

COLLEGE OF OPTICAL SCIENCES

In Partial Fulfillment of the Requirements

For the Degree of

MASTER OF SCIENCE

In the Graduate College

THE UNIVERSITY OF ARIZONA

2022

THE UNIVERSITY OF ARIZONA
GRADUATE COLLEGE

As members of the Master's Committee, we certify that we have read the thesis prepared by **Kimberly Jolene Doty**, titled ***A Modular SPECT Camera Combining PMTs and SiPMs*** and recommend that it be accepted as fulfilling the thesis requirement for the Master's Degree.

Professor Lars Furenlid Date: 12/12/22

Professor Arthur F. Gmitro Date: 12/12/22

Professor Matthew A. Kupinski Date: 12/12/22

Final approval and acceptance of this thesis is contingent upon the candidate's submission of the final copies of the thesis to the Graduate College.

I hereby certify that I have read this thesis prepared under my direction and recommend that it be accepted as fulfilling the Master's requirement.

Professor Lars Furenlid Date: 12/12/22
Master's Thesis Committee Chair
Wyant College of Optical Sciences

ACKNOWLEDGEMENTS

I would like to thank my advisor, Dr. Lars Furenlid, for his guidance and advice throughout this work. I am so grateful for all that you have taught me and I am so glad that you have supported me in getting my M.S. in optics while working toward my PhD in BME. I think we were equally excited about the idea. Thank you to Dr. Matthew Kupinski. I cannot express enough graditude for the amount of time you have spent helping me debug this code. I don't think I could have done it without you. Thank you for your patience as I learned a new coding language and for teaching me how to debug in GPU. I am so glad to have had you as my mentor. Thank you to Dr. Gmitro for serving on my committee and for your help my first few years of grad school.

I would also like to thank my peers, Neil Momsen, Alex Lin, Maria Ruiz, Garrett Richards, Kelsea Cronin, Micaehla May, and Owen Anderson for their advice and friendship. Owen, without your support through classes and our trips for brownies in the cafe I am not sure I would have made it. You are truly a one-of-a-kind friend and I am so glad you have kept me laughing through the pain of graduate school.

More personally, I would like to thank my sister, Tiffany Dillon, for all of the phone calls of emotional support and virtual hugs and motivation. Thank you for all the times you would proof read my writing. To my dear friends I have made along the way: Haley, Jacob, and Daniel thank you for all your love and support. To Zack, Jake, Scott, and Levi, you are truly the greatest and I am so thankful for each of you, I don't know what I would do without our adventures.

And the biggest thank you to Brandon Doty, for his love and support throughout this work. You have helped me celebrate every win and supported me through every struggle and words cannot express how grateful I am.

TABLE OF CONTENTS

TABLE OF CONTENTS – *Continued*

LIST OF FIGURES

LIST OF TABLES

ABSTRACT

In this work, novel modular gamma camera concepts for SPECT imaging systems were investigated. The camera designs included curved scintillation crystal to address parallax errors and 3D position resolution In addition, fiber optics plates as a light guides to transfer scintillation light from the curved exit face of the scintillation crystal to the planar light sensors for readout. The estimated intrinsic spatial resolution of the cameras averaged over the detector volumes were used as the figures of merit for comparisons. Spatial resolution was estimated using the Cramér-Rao lower bound condition from Fisher Information Matrices. The components of the Fisher Information Matrices were derived under an assumption of Poisson statistics by finding mean detector response function using a custom Monte-Carlo photon transport code written in Swift and Metal. All the designs were candidates for the AdaptiSPECT-C system, and ultimately a camera design using a hybrid combination of silicon photomultipliers and photomultiplier tubes balanced cost and performance goals for this system. The addition of curvature into modular gamma cameras did not significantly change the intrinsic spatial resolution of the cameras but does improve the point spread function for oblique rays from a single pinhole collimator. The addition of fiber optic plates as light guides does offer a path to improved 3D positioning that is worth exploring with a prototype camera and point-spread-function measurements.

CHAPTER 1

Introduction

1.1 Drug Discovery in Neurodegenerative Diseases

Despite decades of study, the pathophysiology of most of the major neurodegenerative diseases are not well understood but, current thought is that they may share most of the major mechanisms of inception and development (Dupont et al., 2018). In recent years, there has been some advancement in understanding disease progression of Alzheimer's, Parkinson's, and other neurodegenerative diseases (Benadiba et al., 2012). This group of disorders is increasingly affecting elder generations and the number of persons being treated for these disorders are expected to double every 20 years (Dupont et al., 2018). With slow development, limited or no access to living tissue samples, and variability in disease progression between patients, it is difficult to develop drugs for treatment (Dib, 2005).

New therapeutic treatments have low success rates when going through Phase III clinical trials. Between 2002 and 2012 only one drug for Alzheimer's disease was approved after 413 trials (Bolognesi, 2017). The limited progress in development of new treatments is related to the complexity of disease progression. The pathophysiology that leads to neuronal death is not fully understood and symptoms occur after advanced neuronal loss. For drug development, long observation is necessary to study the difference between those receiving treatment and the controls, as changes are slow to develop. This poses a challenge for drug discovery in addition to the large sample sizes necessary to reach statistical significance due to the high variability between patients' disease progression. Both biochemical and imaging markers are of interest for clinical trials of potential drugs to aid in these challenges (Dib, 2005).

In Alzheimer's Disease, amyloid-β (Aβ) plaques and misfolded tau protein that

forms tangles are the main pathological features (Bloom, 2014). In an effort to target the pathophysiology and prevent disease progression anti-Aβ monoclonal antibodies (mabs) have been developed and are undergoing clinical trials (Shi et al., 2022). One treatment studied was ganternerumab which is a fully human mab that binds and removes AB. In a phase III trial, a significant clinical benefit was not found, but ganternerumab's mechanism of action was confirmed (Ostrowitzki et al., 2017). A study done using positron emission tomography (PET) suggested potential clinical benefit for the removal of Aβ at higher doses (Klein et al., 2019). Another fully human mab that is being studied is lecanemab. An initial study showed that lecanemab was well-tolerated and had shown a reduction in brain amyloid, however, it did not reach an 80% probability of being better than placebo by 25% (Swanson et al., 2021). From intial findings, lecanemab is the most promising treatment for AD showing decline of Aβ levels, higher safety, and the reduction of cognitive decline (Shi et al., 2022).

Positron emission tomography (PET) and single photon emission computed tomography (SPECT) are used as non-invasive methods for tracking molecular targets with connection to neurodegenerative diseases *in vivo* (Benadiba et al., 2012). SPECT and PET can reveal the kinetics of pharmaceuticals in the central nervous system and are used to determine dosage and thresholds for the therapeutic window. These imaging techniques can continue to help elucidate the mechanism of drug treatment and also have the potential to be used to measure efficacy (Benadiba et al., 2012). PET and SPECT can be used to image neurotransmitter disruption as well as glucose metabolism and neuronal loss (Dib, 2005). Radiotracers used for both imaging methods need to cross the blood-brain barrier and must accumulate at the biological target (Benadiba et al., 2012), to be useful as possible markers for neurodegeneration (Dib, 2005).

There is a continuous discovery of underlying mechanisms in neurodegenerative diseases and new molecular targets being developed. Development of molecular imaging radiotracers for these new targets will be imperative for growing insight into the pathological processes that occur in neurodegenerative diseases. Radio-

tracers will be useful to identify, validate, and assess therapeutic targets used for treatment. A useful strategy would be to image multiple molecular targets simultaneously to better understand their interactions with one another (Benadiba et al., 2012). By radiolabling new drugs, the bio-distribution and passage through the blood-brain barrier could be monitored (Dupont et al., 2018). The lower cost and larger availability of SPECT in comparison to PET as well as the ability to image multiple targets make it a favorable choice for the application to drug discovery (Benadiba et al., 2012). The differences between SPECT and PET and the potential advantages of SPECT for certain applications will be discussed in further detail in Chapter 2.

CHAPTER 2

Chapter 2: Gamma-Ray Imaging

2.1 Introduction

Emission tomography with gamma rays is a functional imaging modality. Unlike MRI or transmission X-ray imaging, which image anatomy, nuclear imaging is used to image properties of the subject's physiology or biochemical function. To do so, it relies on the emission of photons from within the body. These photon emissions come from a radioactive atom that is used to label a molecule of interest that targets the biological function being imaged. When the radiotracer undergoes decay, it creates a distribution of measurable radiation. The radiation is then detected externally via an imaging device such as a scintillation camera (Wernick and Aarsvold, 2004).

This chapter describes the physics of emission and conversion of a radioisotope decay into a measurable signal. First, an introduction to decay processes that produce gamma-ray emissions and their interaction with matter will be presented. This will be followed by a description of scintillator crystals and photosensors used in gamma-ray cameras. Next, an explanation of how the gamma cameras are used and a comparison between clinical and modular gamma cameras will be discussed. Finally, gamma-ray imaging techniques, SPECT and PET, will be compared.

2.2 Nuclear Radiation

An atom consists of a nucleus surrounded by electrons. The nucleus is composed of protons and neutrons. The atomic number, Z, defines the element and represents the number of protons in the nucleus. The number of neutrons in the nucleus is represented by N. The sum of the protons and neutrons is represented by A, which is the mass number since protons and neutrons have nearly identical masses very close to 1. An element, X, is denoted as ${}^{A}_{Z}X$.

A unique combination of protons and neutrons in a nucleus is known as a nuclide. If a nuclide undergoes radioactive decay, it is known as a radionuclide. Atoms that have similarities can be isotopes, isobars, isotomes, or isomers. Atoms with the same atomic number but different mass numbers are known as isotopes. Isobars are atoms with the same mass number but different atomic numbers. Those with the same number of neutrons are known as isotones. Isomers are atoms that have the same A and Z but have nuclei in different energy states (Prince and Links, 2006).

Radioactive decay transforms atoms by rearranging the parent isotope's protons and neutrons to have a lower energy, which is known as the progeny isotope. This process releases energy and occurs spontaneously. The unique combinations of protons and neutrons can be classified in two groups; those that are stable and those that are radioactive (radionuclides) (Prince and Links, 2006). The ratio of protons and neutrons in the nucleus create stability or instability. The curve that describes this ratio is known as the line of stability and is shown in Figure 2.1. For atoms with a Z less than 40, stable nuclei have N $\approx$ Z. For heavier atoms this stability tends toward N $\approx$ 1.5Z, but all nuclides that are heavier than ^{209}Bi are unstable. The increase in the ratio of neutrons to protons offsets the increase in the repulsive Coulomb forces between protons for increasing Z. The further a nuclide is from this ratio, the more likely it is to be unstable, and the decay generally transforms atoms into those that are closer to the line of stability (Wernick and Aarsvold, 2004).

The number of atoms undergoing decay per unit of time is called the activity. The SI unit of radioactivity is the Becquerel (Bq) where 1 Bq = 1 disintegrations per second (dps). The common unit is the Curie (Ci) where 1 Ci = 3.7 $\times 10^{10}$ dps. The law of radioactive decay states the loss of radioactive atoms (N) per unit of time is proportional to the number of radioactive atoms given by

$$-\frac{dN}{dt} = \lambda N, \tag{2.1}$$

where λ is the decay constant with units inverse time and is dependent on the radionuclide. This equation can be integrated to calculate the number of radioactive atoms present at time t (N_t) assuming there were N_0 initial radioactive atoms to

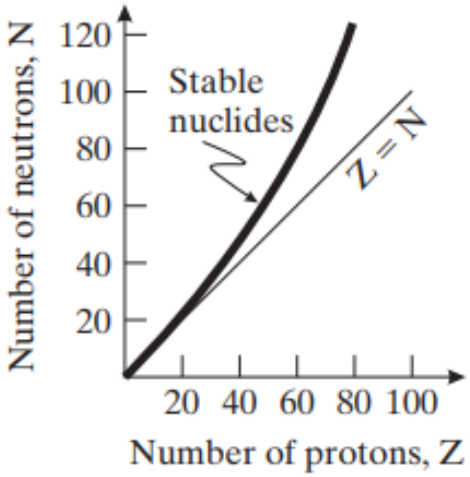

Figure 2.1: The line of stability as a function of protons and neutrons (Prince and Links, 2006).

give

$$N_t = N_0 e^{-\lambda t}. \tag{2.2}$$

The half-life $t_{\frac{1}{2}}$ of a radionuclide is the time it takes for the number of radioactive atoms to decrease by a factor of 2. By using the previous equation and solving for the half-life we find

$$t_{\frac{1}{2}} = \frac{\ln(\frac{1}{2})}{\lambda}. \tag{2.3}$$

The radioactive decay law equation and its derivatives predict the average number of radioactive atoms at a given time. Radioactive decay is a random process governed by Poisson distribution. Poisson statistics requires that each event is independent and rare. For isotopes undergoing spontaneous decay, the decay of one atom does not affect the decay in another atom and for an extremely small time interval, there will only be one disintegration or zero. Therefore the distribution governing the decay of radionuclides during a time interval T is given by:

$$Pr[\Delta N = k] = \frac{(\Delta N)^k e^{\Delta N}}{k!}, \tag{2.4}$$

where ΔN is the number of decays expected on average in a time period T. This equation describes the probability that the number of actual decays equals k and was first derived by Poisson to describe other rare and independent phenomena (Prince and Links, 2006).

2.3 Nuclear Decay Modes

There are four main types of nuclear decay: fission, alpha decay, beta decay, and isomeric transition. Fission is when a nucleus decays into two lighter nuclei. Some fission does occur spontaneously, but typically it occurs when energy is added to a nucleus through the bombardment with neutrons, protons, gamma rays. Alpha decay results in the emission of an alpha particle, which consists of two protons and two neutrons. Beta decay is the transformation of a neutron to a proton or vice versa by either absorption of an electron (β^-), known as electron capture, or emission of an electron or positron (β^+). Electron capture is given by:

$$p + \beta^- \rightarrow n \tag{2.5}$$

and β emission is given by:

$$p \rightarrow n + \beta^+ \tag{2.6}$$

$$n \rightarrow p + \beta^- \tag{2.7}$$

where p is a proton, n is a neutron, β^+ is a positron, and β^- is an electron. A beta particle is thus either an electron or a positron. Isomeric decay occurs when a nucleus is in an excited state (known as metastable) and decays releasing energy in the form of a gamma ray.

2.3.1 Positron Decay

When a nuclide is proton rich, a proton can convert to a neutron via positron emission:

$$p \rightarrow n + \beta^+ + \nu_e \tag{2.8}$$

where p is a proton, n is a neutron, β^+ is a positron, and ν_e is a neutrino. A positron is an antimatter electron with the same mass as an electron but with a positive charge. A neutrino is a very low mass and chargeless spin $\frac{1}{2}$ subatomic particle that serves to balance conserved properties in nuclear decays. A positron decay leads to the emission of two annihilation photons that are both 511 keV through annihilation with an electron. The positron will travel a few millimeters before meeting an electron, and by conservation of energy and conservation of momentum the rest mass of an electron and positron are converted to two coincident high-energy photons that travel in opposite opposite directions (Prince and Links, 2006). The conservation of energy is described by Einstein's famous equation:

$$E = mc^2. \tag{2.9}$$

2.3.2 Gamma-Ray Emission

Gamma-ray emission occurs when the parent nucleus is in an excited state. This means that the nucleus itself has additional energy. The decay of a metastable atom is an isomeric transition because the progeny nucleus has the same Z and N and so the parent and progeny are chemically identical with different energies. The excess energy is released in the form of gamma rays. Metastable radionuclides are useful in nuclear imaging because of their relatively long half-lifes and lack of particle emissions that deliver undesired dose to patients. A common example in nuclear imaging is

$$^{99m}Tc \rightarrow ^{99}\,Tc + \gamma. \tag{2.10}$$

2.4 Nuclear Imaging Radionuclides

In nuclear imaging we most often image using radionuclides that undergo positron emission or gamma-ray emission. Alpha and beta decay isotopes are sometimes used for theranostic" imaging because they can yield image data while also contributing to patient therapy with radiation. A combination of energy emitted and half-life is important when considering which radioisotope to use. A high enough energy is

needed so the gamma ray can leave the body with small amounts of attenuation but it should be low enough to interact with detectors. Also required is a half-life that provides enough time to perform a labeling reaction and collect an image but while remaining short to create enough photon flux to prevent patient motion from becoming a large concern (Wernick and Aarsvold, 2004).

2.5 Interaction With Matter

Photons do not carry an electric charge, but they are propagating electromagnetic fields. This means that photons do interact with electric charges. Most of the interactions are with electrons for photons produced in nuclear decay. The photons transfer their energy to the electrons via two main types of this interaction: photoelectric effect and Compton effect. As a beam of photon travels through matter, it is attenuated by the photoelectric effect and the Compton scatter. This is demonstrated in Beer-Lambert Law given by:

$$I = I_0 e^{-\mu x} \tag{2.11}$$

where I is the intensity of the attenuated beam, I_0 is the incident intensity, μ is the attenuation coefficient, and x is the depth traveled within the material, thus $e^{-\mu x}$ represents the probability of passing through and $1 - e^{-\mu s}$ is the probability of interacting.

2.5.1 Photoelectric Effect

When the gamma-ray photon interacts with a bound electron and the photon transfers all of its energy to the electron and is completely absorbed, it is known as the photoelectric effect. The electron is ejected from the atom and the atom absorbs some of the momentum, conserving energy and momentum as seen in Figure 2.2.

2.5.2 Compton Effect

When the photon interacts with an electron, the photon can also transfer part of its energy and momentum to create a free electron. This is know as Compton scatter.

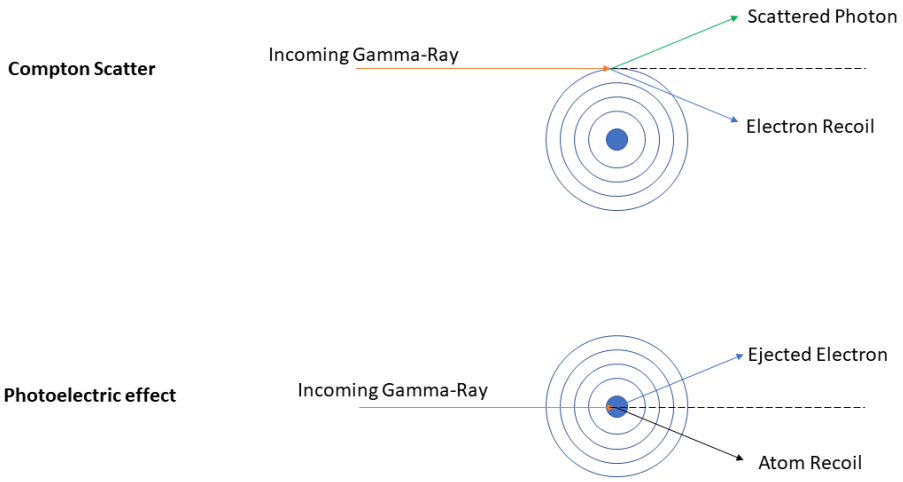

Figure 2.2: An incoming gamma-ray shown in orange interacts with an atom. The top figure shows Compton Scatter when the photon interacts with an outer shell or weakly bound electron. The scattered photon is shown in green and the recoil electron in blue. The bottom figure shows the Photoelectric Effect. In this case the incoming gamma-ray interacts with a bound electron and deposits most of its energy ejecting the electron shown in blue. The atom recoils to preserve the conservation of momentum and energy which is shown in black.

This usually involves outer shell electrons because there are more of them. The photon is not absorbed and retains some energy. The energy of the post-scatter photon is found using:

$$E_f = \frac{E_i}{1 + \frac{E_i}{m_e c^2}(1 - \cos(\theta))} \tag{2.12}$$

where E_f is the final photon energy, E_i is the initial photon energy, m_e is the mass of the electron, c is the speed of light, and θ is the angle at which the photon scatters (Wernick and Aarsvold, 2004). This process is also shown in Figure 2.2.

2.6 Gamma-Ray Imaging

Gamma-ray imaging is a functional imaging modality. Unlike MRI or X-rays, which primarily image anatomy, nuclear imaging is used to image properties of the subject's physiology or biochemical function. To do so, it relies on the tracer principle, which states that radioactive compounds behave the same way as non-radioactive compounds during physiological processes and furthermore that small amounts of introduced tracer molecules do not affect the organism. Photon emissions come from a radioactive atom that is used to label a molecule chosen to highlight the biological function being imaged. When the radiotracer undergoes decay, the photons are detected with an imaging device such as a scintillation camera (Wernick and Aarsvold, 2004).

2.6.1 Tomography

3D gamma-ray imaging uses an image forming process similar to the 2D Radon Transform (Peterson and Furenlid, 2011). Tomography involves projections which are then used to create an image though reconstruction. Data is recorded by the imaging system at many angles around the body. This data is then used to create a 3D volume through backprojection, and stacks of 2D slices along different axes are used to visualize the 3D object (Wernick and Aarsvold, 2004).

2.6.2 SPECT and PET

There are two different types of 3D nuclear medicine imaging; SPECT and PET. One way in which they differ, is in the type of radioisotope used for imaging. SPECT radioisotopes decay to emit one gamma-ray at a time whereas PET radioisotopes decay to release a positron. When a positron is emitted it travels a small distance before encountering a nearby electron, and the two annihilate releasing two coincident gamma-rays (Wernick and Aarsvold, 2004). SPECT probes typically have longer half-lives than PET tracers. This avoids the need for a nearby cyclotron. Common SPECT radioisotopes are iodine-123 (^{123}I) and technetium-99m (^{99m}Tc). The most

used radioisotopes for PET are carbon-11 (^{11}C) and flourine-18 (^{18}F). Carbon-11 must be synthesized in an on-site cyclotron due to a half-live of only 20 minutes. Flourine-18 has a half-life of 110 minutes and once synthesized in a cyclotron can be transported to nearby facilities (Benadiba et al., 2012). Radionuclides that are commonly used are shown in Table 2.1.

Nuclide	Half-life	SPECT or PET	Energy of Gamma Ray(s)
^{11}C	20.3 min	PET	511 keV
^{15}O	2.1 min	PET	511 keV
^{18}F	110 min	PET	511 keV
^{68}Ga	68 min	PET	511 keV
^{99m}Tc	6 h	SPECT	140 keV
^{111}In	2.8 d	SPECT	173 , 247 keV
^{122}I	3.5 min	PET	511 keV
^{123}I	13.3 h	SPECT	159 keV
^{131}I	8.04 d	SPECT	364 keV

Table 2.1: Examples of common radionuclides used in SPECT and PET. Adapted from (Prince and Links, 2006).

SPECT and PET also differ in image-formation principle. SPECT requires the use of an image forming optic such as a collimator since only one gamma ray is emitted at a time. Collimators are discussed in further detail later in this chapter. PET relies on electronic collimation based on the pair of gamma-rays that are traveling in nearly opposite directions and the timing of the detection. When two 511 keV photons are detected almost simultaneously it is likely they were created by the same decay event somewhere along the line between them (Wernick and Aarsvold, 2004).

2.6.3 SPECT Advantages

SPECT can be used with a wide variety of radioligands for discovery and pharmacokinetic studies of promising drugs for neurodegenerative diseases (Benadiba et al., 2012). SPECT can also in principle image multiple radionuclides simultaneously. This is known as dual-isotope imaging and it requires energy resolution to identify

the events from each isotope. An example combination that can be used is ^{99m}Tc (140 keV) and ^{123}I (159 keV). By using SPECT it is possible to assess more than one functional property of a disease (Peterson and Furenlid, 2011).

2.7 Gamma-Ray Detection

Gamma rays are not easily detected in thin detectors due to their high energy, therefore, a gamma camera was invented to collect imaging data. The scintillation gamma camera was developed in the 1950's by Hal Anger. Detection at that time was done with a small scintillation crystal attached to a multiplier phototube that was moved in a raster scan. Anger developed a way to image the gamma rays quickly without scanning by using an image-forming optic. Since gamma rays cannot be imaged with a traditional lens, gamma cameras have a collimator. Anger's first camera used a pinhole as the collimator, a sodium iodide scintillation crystal, and 7 multiplier phototubes (Myers and Wagner, 1974).

There are alternative methods to detecting gamma rays to create an image today. With technological advances, direct detection of the gamma ray and conversion into an electrical signal was made possible with a semiconductor detector. The energy is deposited in the semiconductor material and an electric field is applied to create signal via the movement of electrons and holes. The semiconductor materials commonly used for these detectors is CdTe and CdZnTe. Neither of these materials can be grown to the same size single crystal as sodium iodide scintillation crystals due to imperfections which also decreases detector yield (Peterson and Furenlid, 2011). Camera dimensions are usually limited to a few centimeters. The cooling of the crystal and readout system is optimal for best performance by decreasing the noise via reducing the leakage current. However, the lower temperatures can cause condensation so it is also important to control the humidity inside the cameras (Cronin et al., 2020). Therefore, for this project, only scintillation based gamma cameras were considered.

Today's scintillation gamma cameras are very similar to Anger's design with

a collimator, scintillation crystal, light guide and photomultiplier tubes, or more recently silicon photomultipliers (Myers and Wagner, 1974). These scintillation-based detectors are widely used in clinical and pre-clinical nuclear imaging because of their low cost, larger areas, high gamma-ray stopping power, and fast timing (Li et al., 2019). A scintillation gamma camera is used for this project and the components of the camera will be described.

2.7.1 Collimators

Collimators are required for SPECT imaging since this process cannot rely on line-of-response imaging like PET. Collimators are used to constrain the angles of light entering the detector and establish the mapping between 3D object space and 2D image space. Traditional Anger Cameras use a parallel hole collimator, best described as an assembly of soda straws made of lead. Other collimation types include diverging, slit-slat, pinhole and multi-pinhole collimators (Peterson and Furenlid, 2011). Some examples of are shown in Figure 2.3.

2.7.2 Scintillators

A photon-counting detector system needs to turn the electromagnetic energies of photons into electronic signals. This is the conversion step of gamma-ray detection. When the emitted gamma ray interacts with a scintillation crystal it deposits its energy and is converted to a burst of optical photons by processes beginning with either photoelectric absorption or Compton scatter (Peterson and Furenlid, 2011). The deposition of energy creates a primary high energy electron which can then create secondary ionizations creating many electron-hole pairs. The scintillation light is produced by the de-excitation of the molecular energy levels (Wernick and Aarsvold, 2004). The number of these secondary photons created is usually proportional to the energy deposited. When selecting a crystal it is important to consider the atomic number and the thickness. There are trade-offs such as spatial resolution that may suffer as the detection efficiency improves (Peterson and Furenlid, 2011).

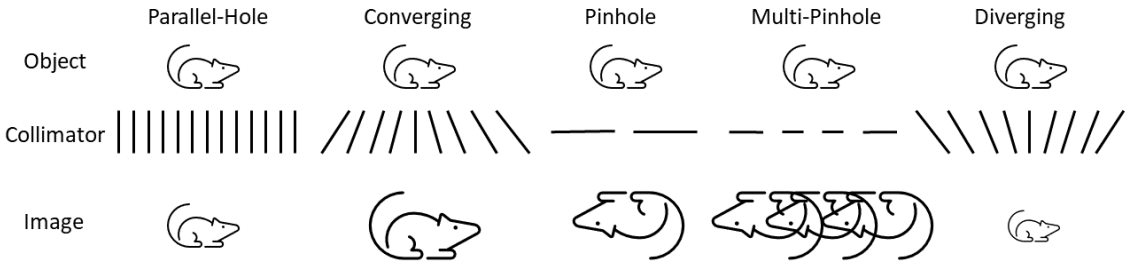

Figure 2.3: Five different types of collimators are shown. Each showing the mapping of the object to the image.

2.7.3 Light Guides

A light guide is made from an optically transparent material and is used to transfer light from the scintillation crystal to light sensors for readout. A variety of materials can be used to match the spectral peak of the scintillation light to improve performance. The light guide is used to allow the light to spread to multiple light sensors. Allowing the light to spread improves the intrinsic spatial resolution of the gamma-ray interaction in the scintillation crystal by creating signals in more sensors (Cherry et al., 2012) (Wernick and Aarsvold, 2004). Increasing the thickness of a light guide increases the uniformity of the spatial resolution, but decreases the energy resolution (Georgiou et al., 2014). Spatial resolution improves between light sensors with thinner light guides, but over the center of light sensors it worsens (Bergqvist, 1998). The properties of the light guide thus represent and interesting optimization problem.

2.7.4 PMTs

In most gamma cameras, photomultiplier tubes are used to detect the optical-wavelength photons that are generated by the gamma-ray interactions in the scintillation crystal. The light strikes the photocathode to generate primary photoelectrons that are then focused and accelerated toward the first dynode. The dynode then releases additional electrons when struck by the primary electrons. The dynodes are arranged in a cascade to multiply the original signal to produce a measurable current. PMTs have a gain factor of around $10^5 - 10^6$ and the current is proportional to the number of scintillation photons that are absorbed. The closest possible packing efficiency with round PMTs and the internal PMT structure are represented in Figure 2.4.

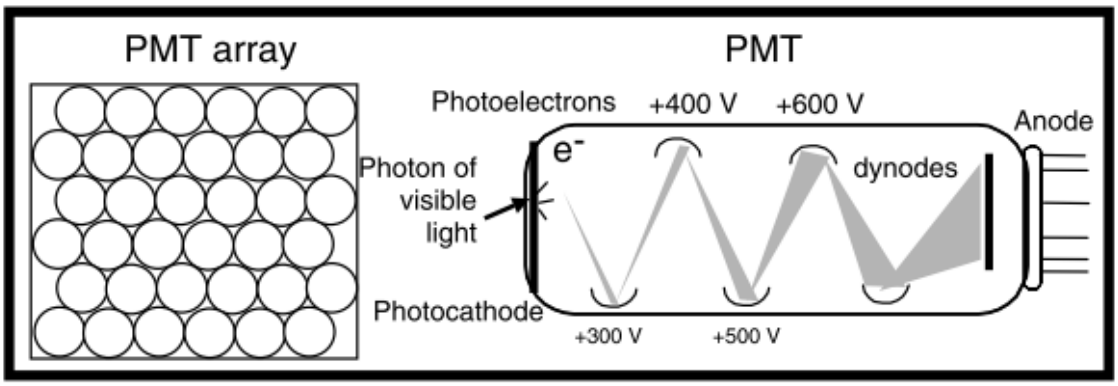

Figure 2.4: A schematic showing the packing arrangement of a PMT and the internal structure (Wernick and Aarsvold, 2004).

The ideal qualities of PMTs are that they produce a measurable current from a single photon providing a good signal-to-noise ratio; that the gain and quantum efficiency are independent of temperature; and that they have a lower cost than other light sensors that are available. The challenges with using PMTs are the low quantum efficiency (around 25 percent), their sensitivity to magnetic fields, and their large size (Wernick and Aarsvold, 2004).

2.7.5 SiPMs

Recently developed silicon photomulipiers can also be used to detect visible photons generated in the scintillation crystal. They use solid state technology. The SiPM uses n+/(p/π)/p+ regions to create an electrical circuit. The π region is a lowly doped p layer between the p and p+ regions. The circuit is set to a reverse bias voltage that is above the breakdown voltage to operate in Geiger mode and create a multiplication region. The n+/p region creates a depletion region in which the avalanche gain occurs (Piemonte and Gola, 2019). When a scintillation photon is absorbed in the p region it creates an electron-hole pair. The electron accelerates toward the n+ region and the holes are traveling toward the p+ region. This leads to high kinetic energy that can create impact ionization, creating a gain in the number electron-hole pairs and thereby the current. They also have a gain of around $10^5 - 10^6$. An external quenching resistor is used to stop the avalanche and return the system to steady state condition in which the it can register the next photon (Saveliev, 2004).

A silicon photomultiplier consists of many of these small circuits known as microcells. A set of microcells are summed to create a single output that is proportional to the number of photons that were absorbed in that area since each microcell is either activated or not in any given time interval. These areas of microcells are then tiled together to create a larger SiPM unit as shown in Figure 2.5

The benefits of using an SiPM are the compactness, higher quatum efficiency, wide sensitivity range, lower sensitivity to magnetic fields, and large fill factors in cameras. The challenges of using SiPMs is the higher cost compared to PMTs, a limited dynamic range, higher background and dark current, and a gain that is sensitive to temperature when using a consistent bias voltage (Piemonte and Gola, 2019). To overcome this it is necessary to monitor temperature and modify the bias voltage as the temperature fluctuates, or regulate the temperature through a cooler and PID controller.

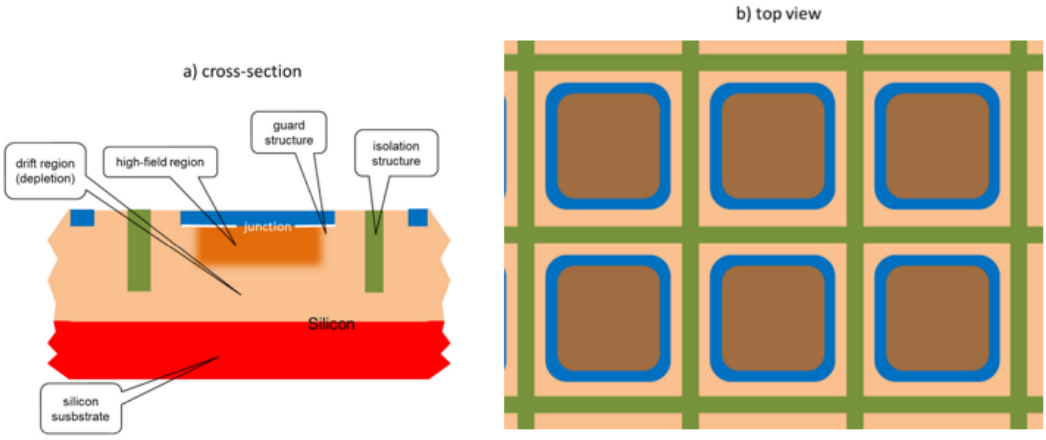

Figure 2.5: A cross section and top view of a single microcell in an SiPM unit adapted from Piemonte and Gola (2019).

2.8 SPECT Detectors

The most important characteristics of a SPECT detector are detection efficiency (sometimes referred to as stopping power), spatial resolution, and energy resolution. A scintillation crystal should have light yields that are proportional to the energy of the gamma rays being imaged. Having good energy resolution allows you to remove data from photons that have scattered and partially deposited energy as well as any x-rays that are generated. An additional benefit of good energy resolution is the capability to simultaneously image more that one radionuclide by sorting each interaction into energy windows and creating complementary images. A camera needs to have good uniformity in spatial and energy resolution. If it is not uniform, then the non-uniformities need to be well defined such that they can be corrected for during reconstruction. A detector must also have a sufficient capacity for high count-rates during calibration and image collection. This can be increased by the use of multiple modular cameras with independent readout (Peterson and Furenlid, 2011).

CHAPTER 3

Chapter 3: System and Camera Design

This chapter describes the human brain imager system known as Adapti-SPECT-C. The motivation for the camera design project and features of the camera design will be discussed. The camera designs described in this thesis are candidates for the Adapti-SPECT-C system or eventual follow-on projects.

3.1 AdaptiSPECT-C

As a system fundamentally designed to capture dynamic data, AdaptiSPECT-C incorporates multiple detectors and multiple pinholes to simultaneously acquire projection data from multiple angles. Its roots are in concepts previously proposed in the 1990's (Rogulski et al., 1993). It is possible to gain sensitivity without sacrificing image resolution using multi-pinhole imaging (Barrett and Kupinski, 2005). Previous work includes FASTSPECT I (Four-dimensional Arizona STationary SPECT), FASTSPECT II, FASTSPECT III, and AdaptiSPECT. FASTSPECT I was also designed for dynamic 3D SPECT imaging of the brain (Klein et al., 1995). FASTSPECT II and III were designed for small animal imaging but built upon previous work with larger-area camera design and improved readout electronics (Furenlid et al., 2004) (Miller et al., 2009). AdaptiSPECT was a small animal imaging system that incorporated adaptive pinholes and task based adaptive imaging schemes (Chaix et al., 2012) (Chaix et al., 2013).

AdaptSPECT-C is a collaboration between the University of Arizona and the University of Massachusetts Medical School. This imager will be used for drug discovery and testing for neurodegenerative diseases including Parkinson's and Alzheimer's. For this reason, it needs to have improved spatial resolution and sensitivity compared to traditional two- or three-headed clinical systems. A rendering

of AdaptiSPECT-C as currently designed can be seen in Figure 3.1.

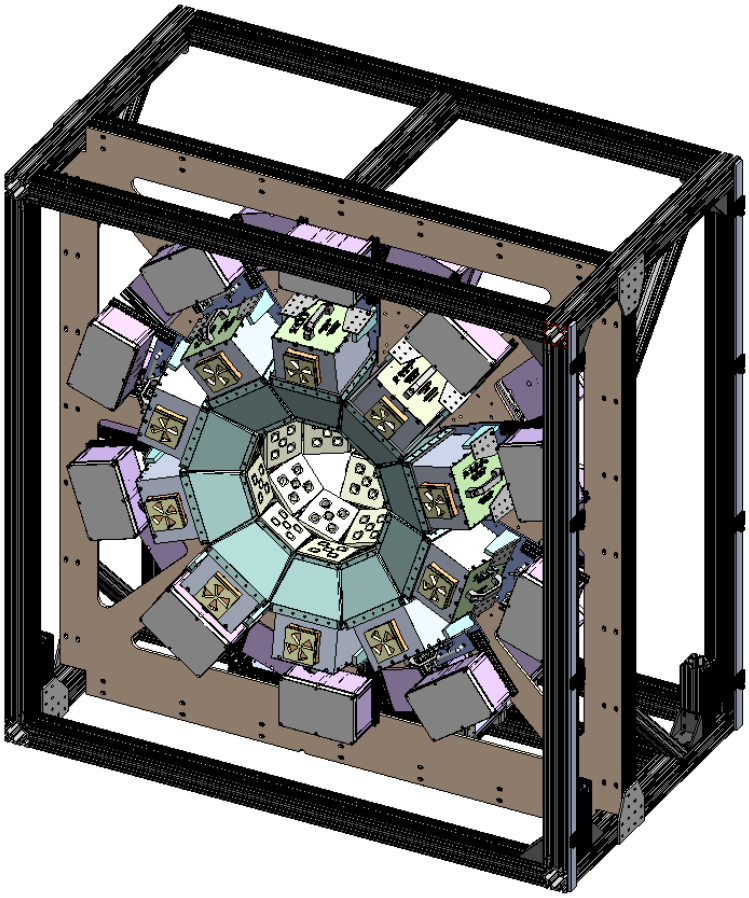

Figure 3.1: Solid Works figure showing AdaptiSPECT-C design. Image courtesy of Garrett Richards.

Conventional two- or three-headed SPECT systems rotate in order to collect the angular sampling needed to reconstruct a 3D image. This rotation and sequential image capture around the subject increases acquisition time in these systems and prevents image collection from being fast enough for ideal 4D imaging. In AdaptiSPECT-C more than 20 modular gamma cameras will be used to concurrently angularly sample the field of view (FOV) without the need for rotation (Richards et al., 2020).

Each of the modular cameras have 5 adaptable pinholes. Each pinhole has

4 possible configurations: low, medium, and high resolution as well as a closed position. Each aperture is individually controlled. This will allow for adaptation of the resolution and sensitivity for best performance based on imaging tasks and activity levels (May et al., 2020). A schematic of the aperture plate and apertures can be seen in Figure 3.2.

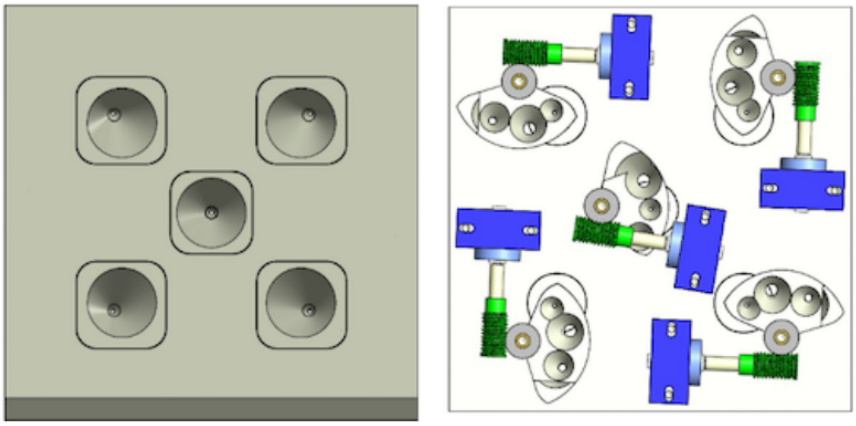

Figure 3.2: A schematic showing the aperture plate and adaptive apertures that will be used in AdaptiSPECT-C (May et al., 2020).

The purpose of this project was to investigate modular camera designs for AdaptiSPECT-C.

3.2 Modular Cameras

Modular cameras are ideal in systems that need high sensitivity. The system count rate is N times that of a single module when N modular cameras are used in a system. Each module is electronically and optically independent (Milster et al., 1990). This is an advantage for system maintenance as it allows modules to be swapped out when repairs or updates to the camera design are made.

There are some disadvantages to using modular cameras. The edges of the crystal do not perform well in conventional scintillation cameras. The point-spread functions (PSFs) become distorted toward the edges and corners of the camera,

resulting in position-estimation errors in these areas that are difficult to correct for (Milster et al., 1990). For the smaller camera faces in modular cameras, this leaves a small amount of detection area in the center where the performance is optimal.

For this project we plan improvements compared to prior SPECT systems by achieving improved camera performance specifically in the corners and edges of the detectors.

3.3 Camera Design

The goal of this project was to find a camera design that met cost and performance goals for Adapti-SPECT-C. Geometry considerations suggested that there was room for 24 cameras in the system. Therefore, careful consideration needed to be taken for the cost and complexity of each individual camera while improving performance. For this project we considered crystal curvature, fiber optic light guides, and novel light-sensor readouts.

3.3.1 Curvature

The curved scintillator design is meant to reduce the parallax error seen in modular gamma cameras when depth of interaction is not estimated. The curvature was conceived for entrance and exit faces of the scintillation crystal and the entrance face of the light guide. By incorporating such curvature, there is a decrease in the size of the PSF on the detector as shown in Fig. 3.3. We considered both a cylindrically and a spherically curved detector. The expense to have this manufactured was important to consider. While the AdaptiSPECT-C system has both on- and off-axis pinholes, a curved detector has the most impact in reducing the parallax error for an on-axis pinhole. The center of curvature and radius we considered are matched to the distance to an on-axis pinhole.

Curvature has been incorporated into some gamma-ray cameras. A group from the University Medical Center Utrecht in The Netherlands created a spherically curved detector. The scintillation crystal was machined from a larger block and was

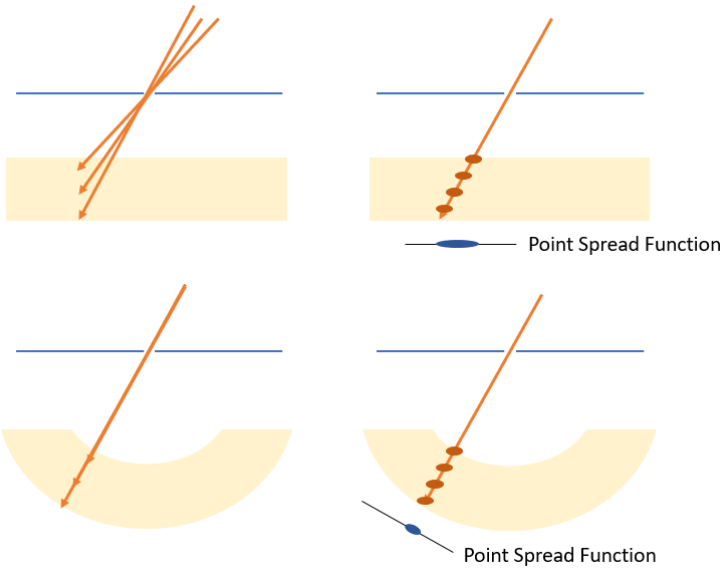

Figure 3.3: Diagram depicting the PSF for a planar and curved detector. The orange arrows represent incoming gamma rays. The orange circles show where the gamma ray can deposit energy. The blue circles show the resulting PSF.

only 20mm in diameter. They used a magnifying fiber-optic taper to transfer the signal to a CCD for readout (Korevaar et al., 2009). Our gamma cameras are much larger and will have a full array of light sensors that tile to equal the size of our camera.

3.3.2 Fiber Optics

The introduction of curvature poses a challenge for planar signal sensors. The planar sensor could be directly optically coupled to the curved surface of the scintillation crystal or light guide (Adam et al., 2001), however, we consider the use of a fiber optic plate that is curvature matched to the light guide on one side and planar on the other side. Upon visual inspection of a 2-inch thick block from InCom, it became evident that the addition of this component will lead to a loss of light.

Fiber optics have been incorporated into both x-ray and gamma-ray detectors in the past. In x-ray detectors, fiber optic tapers have been used to increase the field of

view (FOV) by transferring light from a larger surface to a smaller CCD detector for readout (Tate et al., 1997) (Gruner et al., 2002). In gamma-ray detectors, not only have fibers been used by the group that curved their detector (Korevaar et al., 2009), but they were also incorporated into a small animal SPECT system by a group at the University of Michigan (Meng, 2006). In both of these gamma-ray detectors, the fiber optic tapers were used to take transfer light from a larger surface to a smaller surface similar to how fiber optics have been used in x-ray detectors (Korevaar et al., 2009) (Meng, 2006). In our camera designs the fiber optic plate is used to transfer light with 1:1 magnification.

Fiber optics are characterized by a numerical aperture, this is the maximum incident angle away from normal in which a photon will experience total internal reflection (TIR) as shown in Figure 3.4. The NA is

$$\text{NA} = nsin(\theta_{max}). \tag{3.1}$$

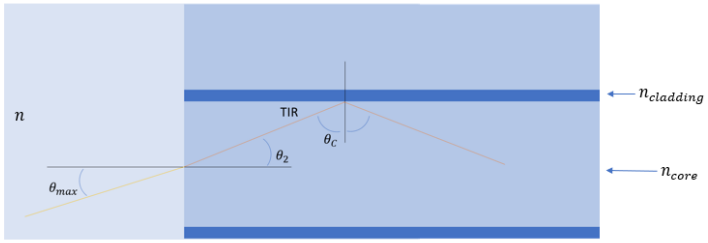

Figure 3.4: Diagram depicting the NA of a fiber optic core for a photon to undergo TIR.

Fiber optic plates typically use step fibers which have a step-like function change in the index of refraction between a higher index-of-refraction core and a lower index cladding. The maximum angle that can enter a core and experience TIR is calculated as

$$\theta_{max} = arcsin(\frac{\sqrt{n_{core}^2 - n_{clad}^2}}{n}). \tag{3.2}$$

A photon that enters the fiber core at an angle less than θ_{max} will experience TIR down the entire length of the fiber core (Cvijetic and Djordjevic, 2013). Those that

do not can be refracted into the fiber cladding and can further refract into adjacent fibers.

3.3.3 Light Detection

A decrease in resolution at the edges of a scintillation detector makes the usable area of a clinical gamma camera smaller than the crystal dimensions. In an effort to reclaim the detector edges, we investigated several light-detector readout configurations. SiPMs are generally more expensive than PMTs, but due to their ability to be subdivided into small areas of readout and higher photon detection efficiency (PDE), we hypothesize that they can produce improved resolution. We looked at using only PMTs, which is the traditional and least expensive gamma camera design. We also considered using all SiPMs, which is the most expensive configuration. And we considered a hybrid model that combines SiPMs and PMTs for readout. For both the full SiPM configuration and the hybrid model, we also considered subdividing the SiPMs into smaller areas for the edges and corners of the camera. Because there is a loss of position-sensitivity when directly above a light sensor, this provides the opportunity to improve resolution at the edges by increasing the light sampling (Milster et al., 1990). This is further discussed below.

CHAPTER 4

Chapter 4 Simulation Method

The camera design candidates were compared via a scintillation-photon simulation code written in Swift, with the computationally taxing component performed in GPU using code written in Metal. Swift (Apple Developer, 2022b) and Metal (Apple Developer, 2022a) are recently developed computer languages that combine properties of C, C++, and Python (Swift) and CUDA (Metal). This simulation code includes index refraction of materials, boundary geometry including radius of curvature, detector size, fiber-plate indices and sizes of the cores and cladding. The basic design included a Lambertian reflector at the entrance face of the crystal, a light guide, an entrance face to the sensors that were simulated by a second light guide, and photo-sensors. All edges were treated as blackened.

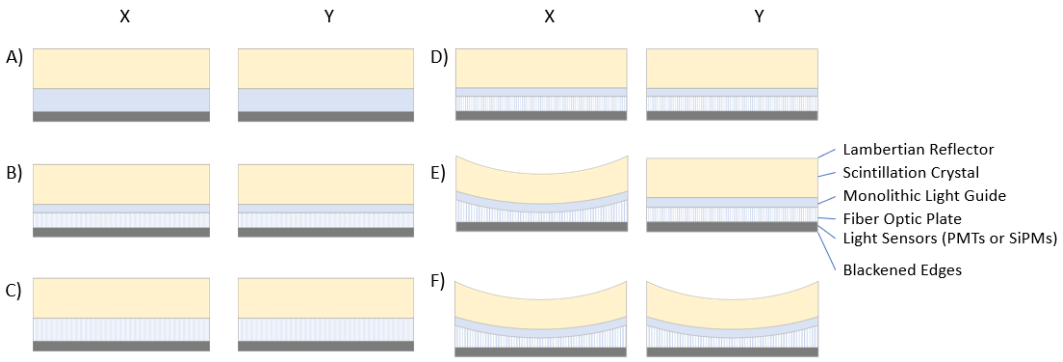

Figure 4.1: This schematic is showing the x and y profiles of the 6 detectors that were tested. The planar detectors on the left (A-C) were used to study the effects of fiber optics and the detectors on the right (D-F) were used to determine the effects of curvature on the intrinsic spatial resolution.

4.1 Monte-Carlo Simulation

The purpose of this code was to carry out a Monte-Carlo simulation of a scintillation detector to produce an estimation of the Mean Detector Response Function (MDRF). To do so, one million scintillation photons are generated from initial gamma-ray interaction positions and ray traced through the detector until reaching a light sensor or being absorbed at an edge. The initial positions span the crystal in the x and y directions in a grid with 1 mm spacing. This was repeated for multiple depths within the crystal in 2 mm increments starting at a depth of 1 mm. Some example trajectories are shown in Figure 4.2.

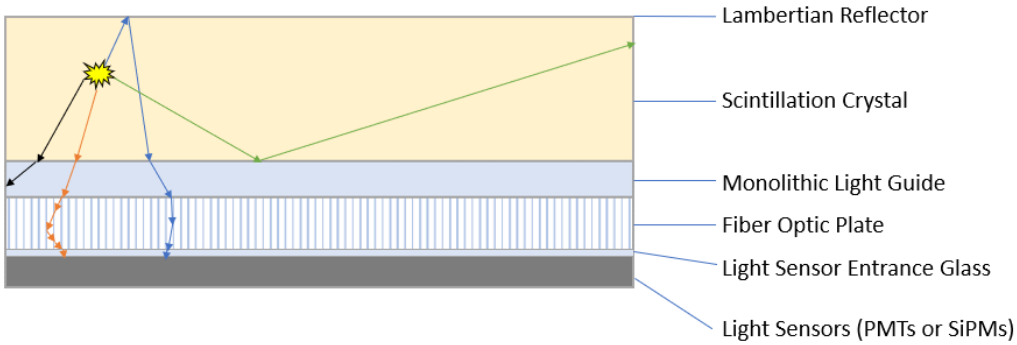

Figure 4.2: This schematic shows some example trajectories in the Monte-Carlo simulation. The black trajectory shows a photon that enters the monolithic light guide and is absorbed at the edge of the detector. The orange trajectory shows a photon that enters the fiber optic plate and refracts between adjacent fibers. The blue trajectory shows a photons that is first reflected by the Lambertian reflector and ultimately enters the fiber optic light guide and TIRs in a single fiber. The green trajectory shows a photon that is reflected within the scintillation crystal and is absorbed at the crystal edge.

The scintillation photons are randomly launched isotropically across the 4π solid angle. The propagation of each photon is then tracked in x, y, and z locations and directions. The front surface is a Lambertian reflection layer. Photons that interact with this surface are given a new random direction vector within a 2π solid angle redirecting the photon back within the scintillation crystal.

4.1.1 Reflection and Refraction

At interfaces where materials of different indexes meet, the probability of reflection or refraction is calculated. The refraction is modeled using Snell's law given by:

$$n_1 \sin(\theta_i) = n_2 \sin(\theta_f) \tag{4.1}$$

where n_1 is the index of the material the photon is in, n_2 is the index of the material the photon could enter, and θ_i is the angle between the normal to the interface and the photon's trajectory and θ_f representing the new angle between the photon's trajectory and the normal to the interface. Reflection and refraction are shown in Figure 4.3.

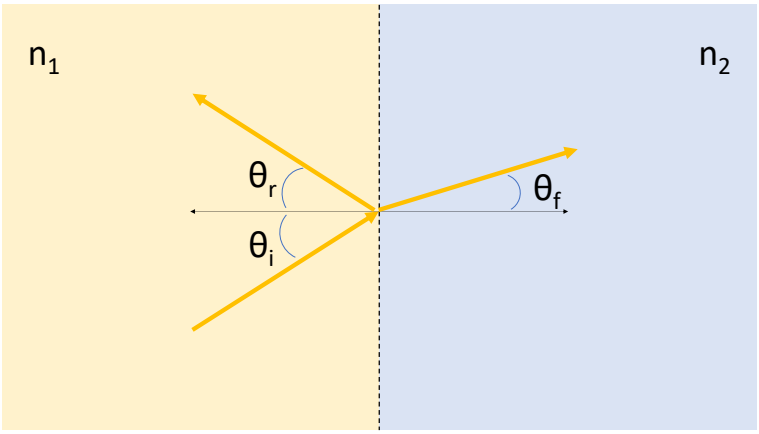

Figure 4.3: Diagram depicting reflection and refraction. In reflection, the photon exits at θ_r and $\theta_r = \theta_i$. In refraction, the photon exits at θ_f.

The fraction of photons reflected for s and p type polarized photons are given according to Fresnel equations (Born and Wolf, 1980):

$$R_s = \left| \frac{n_1 \cos(\theta_i) - n_2 \sqrt{1 - \frac{n_1}{n_2}(\sin(\theta_i))^2}}{n_1 \cos(\theta_i) + n_2 \sqrt{1 - \frac{n_1}{n_2}(\sin(\theta_i))^2}} \right| \tag{4.2}$$

$$R_p = \left| \frac{n_2 \cos(\theta_i) - n_1 \sqrt{1 - \frac{n_1}{n_2}(\sin(\theta_i))^2}}{n_2 \cos(\theta_i) + n_1 \sqrt{1 - \frac{n_1}{n_2}(\sin(\theta_i))^2}} \right| \tag{4.3}$$

where R_p and R_s is the fraction of photons reflected of p and s type respectively, n_1 is the index of the material the photon is in, n_2 is the index of the material the photon could enter, and θ_i is the angle between the normal to the interface and the photon's incident trajectory. The difference between s and p polarization is shown in Figure 4.4. However, since scintillation light is unpolarized, meaning it has equal parts of s and p polarized light, the probability of each is averaged to produce $R_{reflection}$. The order of computations is as follows: First Snell's law is checked to determine if a photon will be reflected via total internal reflection (TIR). If θ_i is greater then the critical angle, then the photon will TIR. If it is less than the critical angle, the Fresnel equations are evaluated to determine the probability of reflection. After calculating the probability of reflection, a uniform random number generator is used to produce a number between 0 and 1. If this number is less than $R_{reflection}$, the photon is reflected, otherwise, the photon is refracted and Snell's law is applied to compute the new direction. Reflection at interfaces, other than at the entrance face and edges, is modeled as specular reflection.

4.1.2 Absorption

The final possible interaction a photon can have while propagating though the detector is absorption. To simulate blackened edges any photons that reach the edge of the crystal, light guide, or fiber optic plate is considered absorbed and it's propagation is terminated. If the photon reaches the entrance face of the PMT or SiPM and is reflected, it is considered lost and modeled the same as absorption in which the photon propagation is terminated and the next scintillation photon is traced.

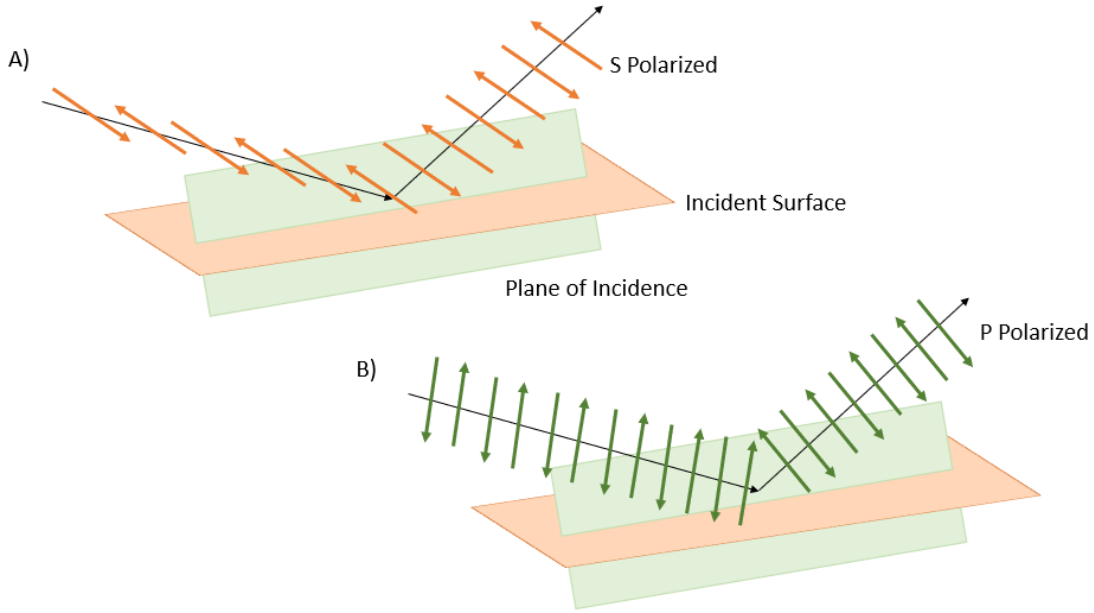

Figure 4.4: This figure shows the difference between s and p polarized light. A) S polarization is when the electric component of the electromagnetic wave is in the same plane as the incident surface. B) P polarization is when the electric component of the electromagnetic wave is parallel with the plane of incidence.

4.1.3 Fiber Optic Plate

The fiber optic plate is modeled as a honeycomb of circular cores and hexagonal cladding as depicted in Figure 4.5. The propagation of the photons through the fiber optics could have been done with wave optics or ray optics. We are able to use ray optics because the diameter of the fiber optic cores are 23 microns and the peak emission wavelength from the scintillation crystal is 0.415 microns (Saint-Gobain Crystals, 2020). When a photon interacts with the interface between the core and the cladding, the probability of reflection and refraction is calculated the same way as at other interfaces. Photons may enter the core or the cladding of the fiber optic plate from the light guide. Once a photon reaches the end of the fiber optic plate it is determined if it enters the entrance face of the light sensor. If a photon is reflected

and therefore does not enter the light detector, the photon is considered lost.

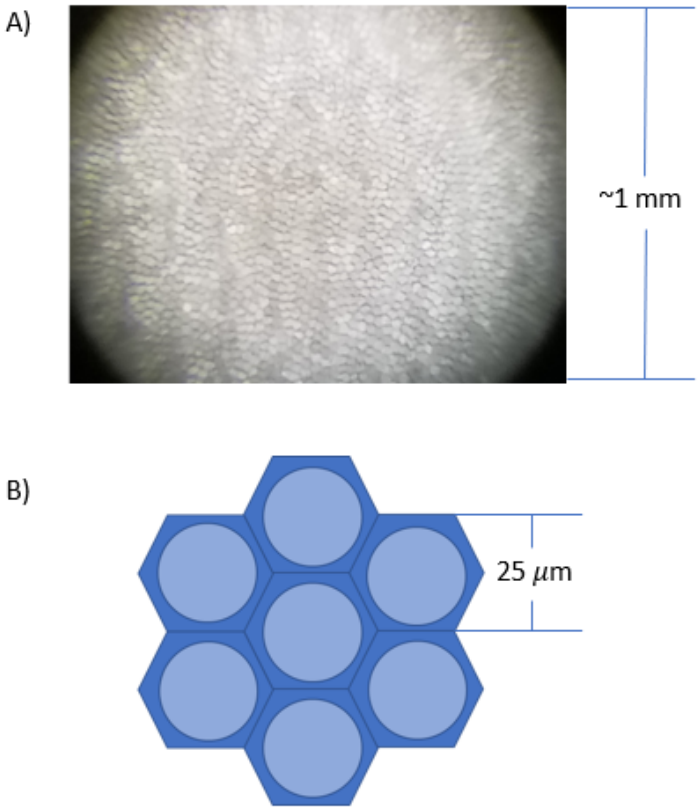

Figure 4.5: In figure A, we can see view of the fiber optic plate under a microscope while back lit. Figure B is a diagram depicting the honeycomb structure modeled for the fiber optics. The core is shown in the lighter color surrounded by the cladding shown in the darker color.

Photons are sometimes able to travel between fibers to enter neighboring fibers as shown in Figure 4.6. We can see this photon travels less than an inch from its initial x,y position as it travels down the 5-mm fiber optic. The curvature of the fiber cores act as a series of lenses as the photon moves to adjacent fibers in the x,y plane which is easier to see in the zoomed in plot of Figure 4.6. If a photon enters the core within the NA of the fiber, then it will experience TIR and travel down the length of the fiber as shown in Figure 4.7. This effect was used to decrease the number of calculations that were used to propagate a photon down the length of a

fiber optic core. The reflections are predictable and the final photon position within the core was calculated and the photon was moved to the exit plane of the fiber optic plate.

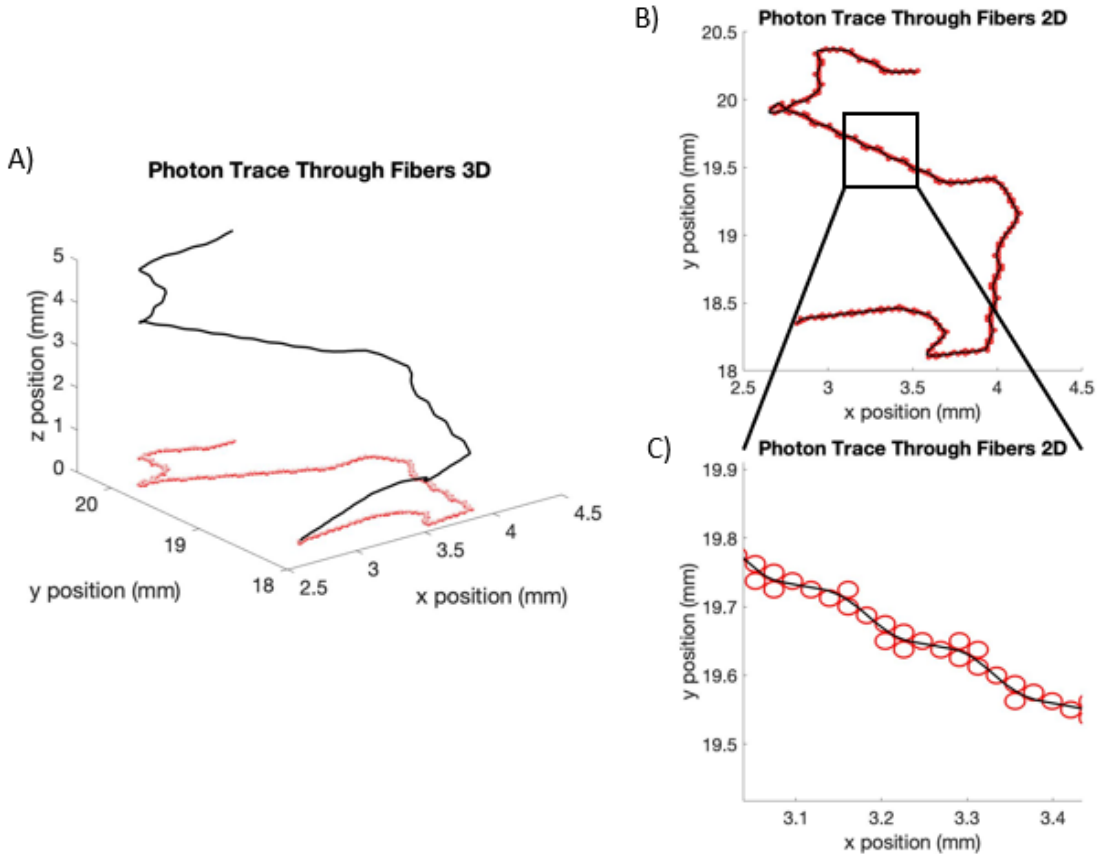

Figure 4.6: This figure was generated by tracking a selected photon's trajectory through the fiber optic plate. The photon trajectory is shown in black and the cores that the photon interacted with is shown in red circles. A) The overall 3D path. B) The 2D path in the x,y plane. C) A zoomed view of the section shown in figure B to show the photon path when traveling between fiber cores.

4.1.4 Photon Detection

For the photon detection, the sensors were simulated to have a 1-mm entrance window of glass. Once a photon traversed the entrance glass, the photon count for

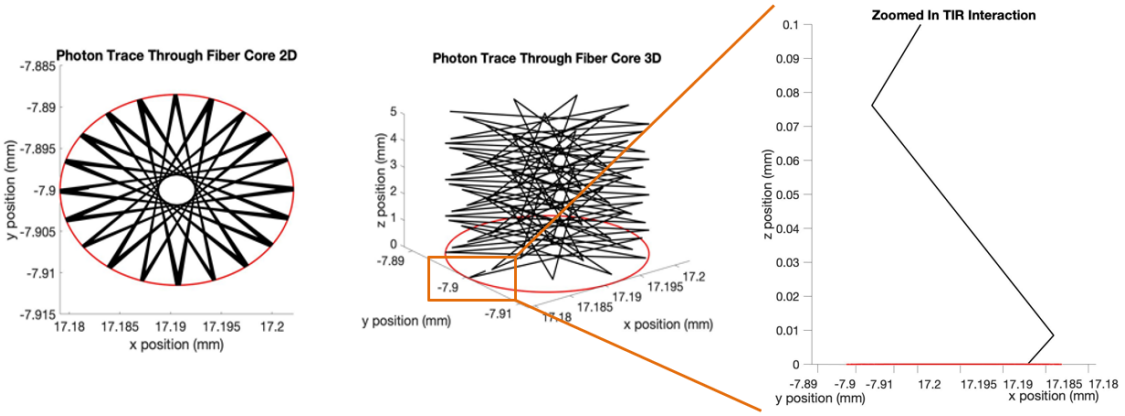

Figure 4.7: This figure was generated by tracking a photon through a single core of the fiber optic plate code. The photon trajectory is shown in black and the fiber core in a red circle. We can see this photon entered within the NA of the fiber and experiences TIR for the entire 5 mm of z-direction travel.

a sensor was incremented by one based on the final x,y position. The quantum efficiency of the sensors could be accounted for at this point in the simulation by rejecting counts. However, due to the time required for a simulation it was advantageous to count all of the photons and account for the quantum efficiency by scaling during analysis. This allows for an easier comparison of the effects of quantum efficiency without requiring starting from scratch. Not included in the simulation for the SiPM sensors were dark current, readout noise, and excess noise as these factors are dependent on operation conditions and vary with manufacturer.

4.1.5 Output

The output of the code is the mean detector response function (MDRF) expressed as the number of scintillation photons that arrive at each scintillation-light detector when 1 million photons are emitted isotropically at a gamma-ray interaction location. Here the detector is the light sensor used in the camera such as a PMT or SiPM. The MDRF shows the photons received in a sensor as a function of the initial position within the crystal. An example MDRF is shown in Figure 4.8 for both an

SiPM and a PMT, with typical quantum efficiencies modeled.

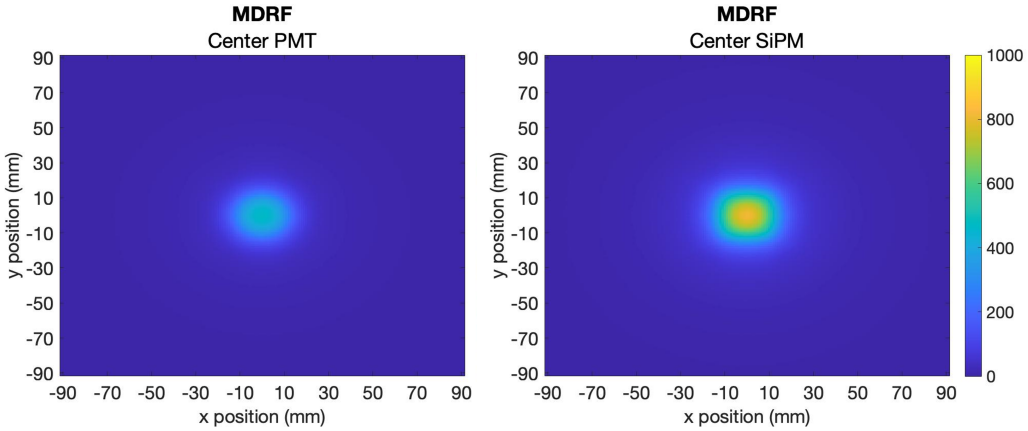

Figure 4.8: Output of the simulation code shown for a PMT and an SiPM in the same position. Typical quantum efficiencies of 0.25 and 0.40 for PMTs and SiPMs; respectively, were used when generating this figure.

4.2 Simulation Details

Photons were launched on a 1 mm x 1 mm x 2mm grid in x,y, and z respectively with each z position sampled pairwise with a separation of ± 0.25mm. At each initial position 1 million photons were launched to get smooth MDRFs. For NaI(Tl), it is expected that a single gamma-ray event will produce a total of 5600 photons given a 140 keV gamma ray and a light yield of 40 photons/keV. The performance was conservatively evaluated with an expectation of 5000 photons from a single 140 keV gamma-ray interaction.

Many camera design features were considered for this project. The effects of adding curvature, fiber optics, and novel combinations of SiPMs and PMTs were investigated. However, we only considered a camera size of 183 mm $\times$ 183 mm (7" $\times$ 7"), as set by the design of AdaptiSPECT-C.

The crystal had an index of refraction of 1.82. The lambertian reflector had a reflectance of 95%. The light guide was modeled with an index of 1.55. These parameters were used for all designs. For the curved scintillation crystals, a radius

of curvature of 305 mm in the x-direction for cylindrically curved was used, and in the x- and y-direction for the spherically curved. A radius of 1,000,000 mm was used for a planar scintillation camera. We included a fiber optic plate that was 16.5 mm thick to accommodate the radius of curvature of 305 mm. We did this to ensure that after curvature matching to a light guide there would be at least 3mm of material to maintain the integrity of the fiber optic plate, and match the 3 mm thickness used for the planar camera. The curved design is meant to reduce the depth of interaction and parallax errors seen in modular gamma cameras. We found a suitable fiber optic plate available from InCom that had a core with a diameter of 0.023 mm and an index of refraction of 1.59 and a cladding with a diameter of 0.025 mm and an index of refraction of 1.49 (Incom, 2022).

We simulated several layout configurations of SiPMs and PMTs. We considered SiPM and PMT configurations as well as a hybrid layout. For these designs a 25.8 mm $\times$ 25.8 mm SiPM unit was used. This SiPM unit is made up of an 8 $\times$ 8 array of 3 mm $\times$ 3mm SiPMs with their own electrical signal (Photonics, 2022). This gives us the ability to sum the data from each channel to form a larger unit or keep each separate. Due to the typically decreased positioning performance at the edges of gamma cameras, we have chosen to increase the sampling by subdividing 1" $\times$ 1" SiPMs into halves along the edges and into quarters at the corners in a single unit for the hybrid and fully SiPM configurations as shown in Figure 4.9.

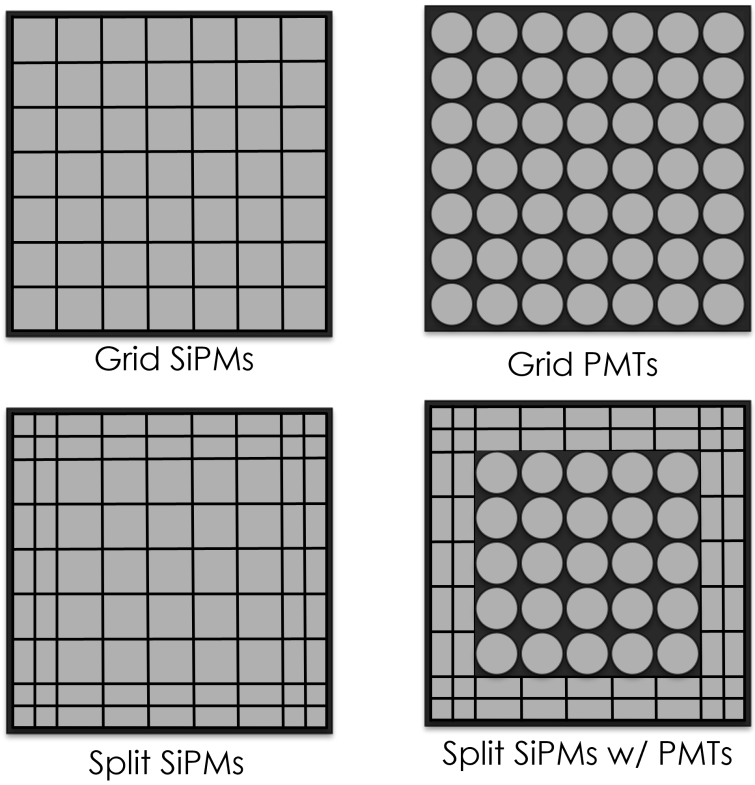

Figure 4.9: The light sensor configurations used for all sizes and the light sensor configurations used for just the smallest and the largest camera.

CHAPTER 5

Chapter 5 Analysis, Results and Future Work

5.1 Analysis

The analysis of the data produced in these simulations was performed in Matlab. The figure of merit (FOM) used to compare designs was the predicted resolutions from the Fisher Information Matrix averaged across the camera face.

5.1.1 Maximum Likelihood

The number of gamma-ray photons emitted during a fixed time interval due to radioactive decay is governed by Poisson statistics. The conditions that lead to a Poisson distribution are: 1) that there is a countable outcome such that a decay event either occurs or it does not; 2) there is rarity such that within a sufficiently small time interval, two decays will not occur, and 3) that each decay event is independent neither encouraging nor suppressing a subsequent event. The detection of scintillation light in photo-sensors is also Poisson for the scintillators considered in this work.

$$Pr(g_m|\bar{g}_m)) = \frac{e^{-\bar{g}_m}(\bar{g}_m)^{g_m}}{g_m!} \tag{5.1}$$

The probability law is shown in Eq.5.1 where g_m is the result of a single experiment and $\bar{g}_m$ is the mean value, for the number of scintillation photons recorded in light sensor m.

For multiple sensors, the probability for all data for the detectors is the product of the probabilities for single sensors, because each g_m is statistically independent, as shown in Eq.5.2 where the bold indicates a set of M signals.

$$Pr(\boldsymbol{g}|\bar{\boldsymbol{g}}(E,x,y,z)) = \prod_{m=1}^{M} Pr(g_m|\bar{g}_m(E,x,y,z)) \tag{5.2}$$

The $\boldsymbol{g}$ is the set of data and $\bar{\boldsymbol{g}}(E,x,y,z)$ is the MDRF for a gamma-ray interaction at (x,y,z) with energy E.

The maximum-likelihood estimate is found by performing a search over the variables to find the maximum value:

$$\hat{E},\hat{x},\hat{y},\hat{z} = \underset{E,x,y,z}{\operatorname{argmax}}[Pr(\boldsymbol{g}|\bar{\boldsymbol{g}}(E,x,y,z))] = \underset{E,x,y,z}{\operatorname{argmax}}[ln(Pr(\boldsymbol{g}|\bar{\boldsymbol{g}}(E,x,y,z)))]. \quad (5.3)$$

Again, the $\boldsymbol{g}$ is the set of data and $\bar{\boldsymbol{g}}(E,x,y,z))$ is the MDRF. The energy is represented by E and the 3D position is x,y,z. The hat indicates an estimated quantity.

5.1.2 Fisher Information

This Fisher Information is directly related to the likelihood functions that describe the relationships between observed data and the physical variables. It can be used to estimate the intrinsic resolution of the camera based on the MDRF simulations that were created. The Fisher Information Matrix (FIM) measures the curvature of the likelihood curves to determine the resolution near the maximum likelihood estimate. The smaller the radius of curvature, the higher the Fisher Information and the better the intrinsic resolution of the camera, as shown in Figure 5.1.

For a likelihood model that considers x,y, and z position only, the FIM is represented by:

$$F = \begin{Bmatrix} F_{xx} & F_{xy} & F_{xz} \\ F_{yx} & F_{yy} & F_{yz} \\ F_{zx} & F_{zy} & F_{zz} \end{Bmatrix} \quad (5.4)$$

For the special case of Poisson statistics, it is straight forward to show that the elements of the FIM are given by:

$$F_{ij} = \sum_{m=1}^{M} \frac{1}{\bar{g}_m(x,y,z)} \frac{\partial\ \bar{g}_m(x,y,z)}{\partial i} \frac{\partial\ \bar{g}_m(x,y,z)}{\partial j}. \quad (5.5)$$

where i and j can be x,y, or z. $\bar{g_m}(x,y,z)$ is the mean response of the m^{th} sensor to events at position x,y,z.

The diagonal elements of the inverse of the FIM are directly related to the lower bound on variances of estimates of x,y, and z position.

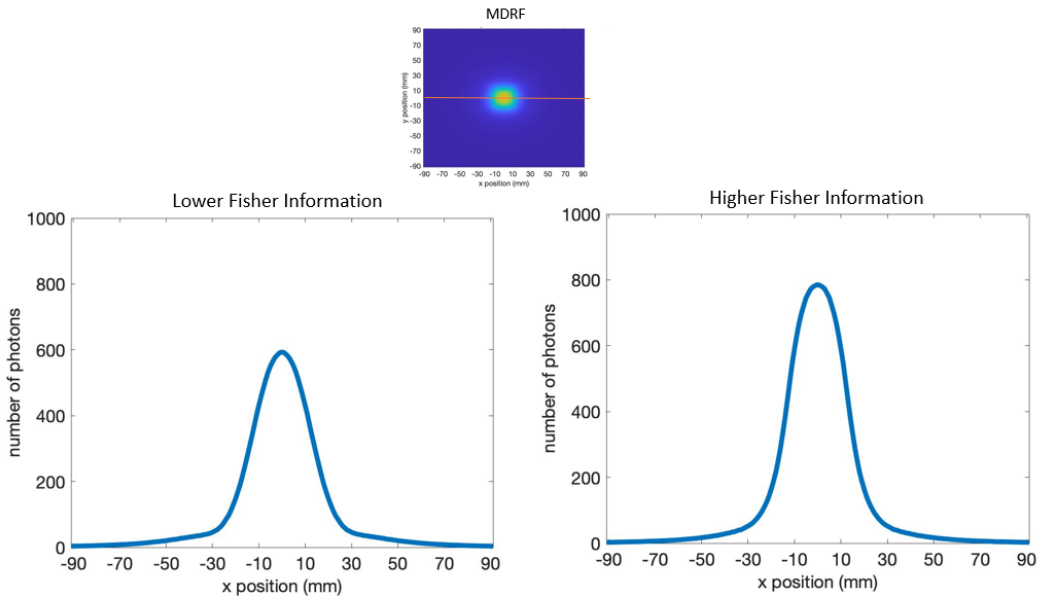

Figure 5.1: The Fisher Information depends on the height and the slope of the MDRF curves as a function of location on the camera face. Shown here are two MDRFs that demonstrate lower (A) and higher (B) Fisher information. The profiles are shown for y = 0 for the center SiPM.

$$[F^{-}1]_{xx} \leq \mathrm{Var}_{xx} = \sigma_{xx}^2 \tag{5.6}$$

$$[F^{-}1]_{yy} \leq \mathrm{Var}_{yy} = \sigma_{yy}^2 \tag{5.7}$$

$$[F^{-}1]_{zz} \leq \mathrm{Var}_{zz} = \sigma_{zz}^2 \tag{5.8}$$

We can use this to estimate the expected resolution lower bound for the simulated camera via the Cramér Rao condition (Barrett et al., 2009).

$$\Delta x \approx 2.35\sqrt{\sigma_{xx}^2} \tag{5.9}$$

$$\Delta y \approx 2.35\sqrt{\sigma_{yy}^2} \tag{5.10}$$

$$\Delta z \approx 2.35\sqrt{\sigma_{zz}^2} \tag{5.11}$$

We used the resolutions averaged over the camera face as the figure of merit that was compared between camera models.

5.1.3 Beer's Law

Since several depths were simulated for each system design, we weighted the resolutions according the the percentage of gamma rays that were stopped in depth zones. Beers law states:

$$I = I_0 e^{-\mu t} \tag{5.12}$$

where the I_0 is the initial number of photons, I is the remaining number of photons, μ is the attenuation coefficient and t is the thickness of the material. For a NaI crystal, the μ value is 2.2413 per cm for a ^{99m}Tc gamma-ray (Ermis and Celiktas, 2015). The crystal was broken down into 2 mm thick zones to best approximate the performance as shown in Figure 5.2.

Figure 5.2: This schematic shows the 4 zones the scintillation crystal was sampled for the MDRFs. The black lines separate the 2 mm zones. The blue lines show the four depths that were sampled pairwise using the depths shown with orange dashed lines.

Each depth simulation was weighted by the percentage of photons that were stopped in each zone by multiplying by

$$\frac{\text{percentage stopped in zone}}{\text{total percentage stopped in crystal}}$$

and summing all of the zones. The resolution as a function of depth is reported as the average over all x, y positions.

Zone	Fraction Stopped	Fraction Remaining	Percentage Stopped
Zone 1	$N_{s1} = 1 - e^{-\mu t}$	$N_{r1} = e^{-\mu t}$	36.15
Zone 2	$N_{s2} = N_{r1}(e^{-\mu t})$	$N_{r2} = N_{r1} - N_{s2}$	23.08
Zone 3	$N_{32} = N_{r2}(e^{-\mu t})$	$N_{r3} = N_{r2} - N_{s3}$	14.74
Zone 4	$N_{s4} = N_{r3}(e^{-\mu t})$	$N_{r4} = N_{r3} - N_{s4}$	9.41
Total			83.38

Table 5.1: This shows the calculations of the percentage of gamma rays that are stopped in each 2 mm crystal zone for an 8 mm thick crystal and the percentages that were calculated.

5.1.4 Point Spread Function

Another way the results of the MDRFs were analyzed was inspection of the point spread function at a grid of locations on the camera face. The point spread function is defined as the intensity distribution of an image of a point source with unit intensity (Rossmann, 1969). The formula used to calculate the PSF was the 2D normal distribution given by

$$\mathrm{PSF}(x,y) = \frac{1}{2\pi\sqrt{1-\rho^2}} e^{-\frac{1}{2\sqrt{1-\rho^2}}[(\frac{x-x_0}{\sigma_x})^2 - 2\rho(\frac{x-x_0}{\sigma_x})(\frac{y-y_0}{\sigma_y}) + (\frac{y-y_0}{\sigma_y})^2]} \tag{5.13}$$

where ρ is the correlation coefficient, σ^2 is the variance, and x_0 and y_0 are the center coordinates of the point spread function (Hamedani and Tata, 1975). The correlation coefficient was found using the off-diagonal elements of the FIM. This was done for an 21 x 21 grid of points in the x,y plane as shown in 5.3.

5.2 Results

We ran simulations to determine the effects of the curvature, fiber optics, and find the light sensor configuration with the best possible intrinsic spatial resolution. The detectors evaluated were a planar detector with a monolithic light guide, a planar detector with a combined monolithic and fiber optic plate light guide, and a planar detector with a fiber optic light guide. We also investigated a cylindrically and a spherically curved detector with a combined monolithic light and fiber optic plate

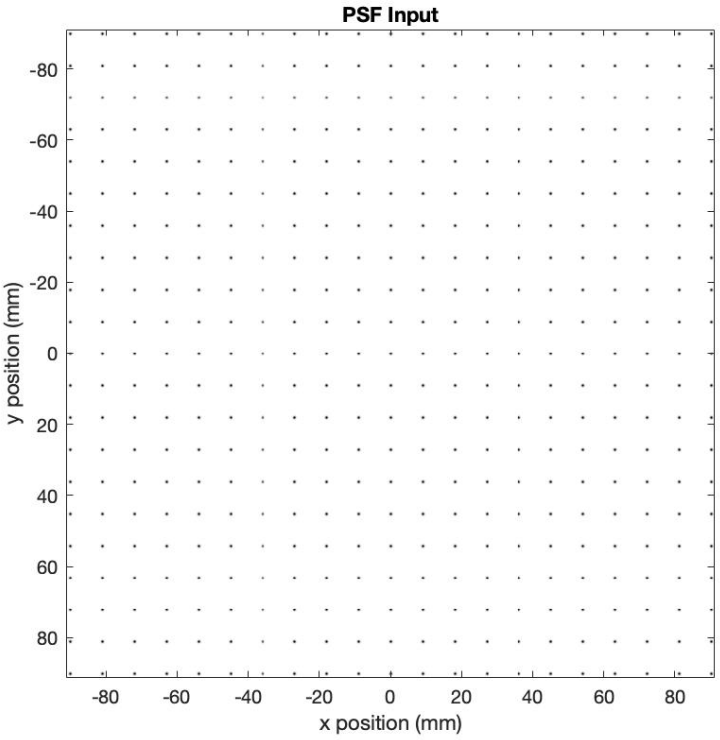

Figure 5.3: This schematic shows the grid of points for the PSF plots.

light guide, and compared the performance with the planar detector that had a combined monolithic and fiber optic light guide as shown in Figure 5.4.

5.2.1 Curvature

When determining the effects of curvature on the intrinsic resolution of the detector, we compared a cylindrically curved and spherically curved scintillation crystal and light guide with the fiber optic plate to a flat detector that also had a fiber optic plate as shown in Figure 5.5. Since the photons that were simulated were initiated in the scintillation crystal, we hypothesized that the resolution should be similar to that expected from the flat detector. Significant resolution improvement would be on the reduction of parallax error during reconstruction where the DOI error would be reduced by the curvature.

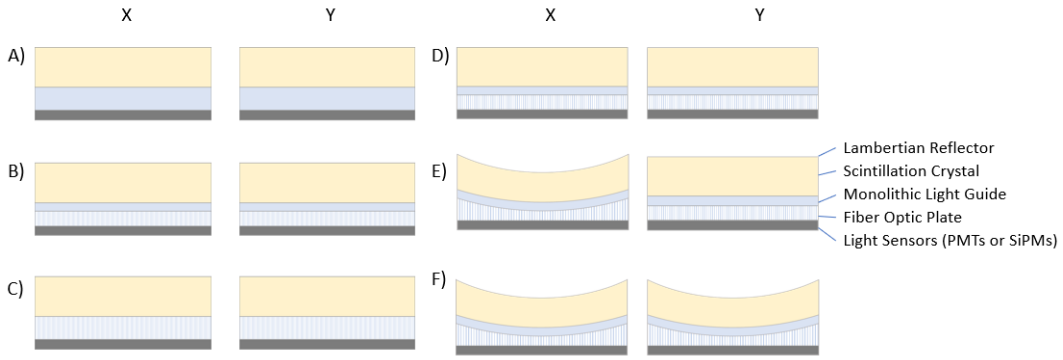

Figure 5.4: This schematic shows the x and y cross sections of the 6 detector configurations that were tested. The planar detectors on the left (A-C) were used to study the effects of fiber optics and the detectors on the right (D-F) were used to determine the effects of curvature on the intrinsic spatial resolution.

The effects of curvature are seen when looking at the profiles of the MDRFs. The curvature decreases the number of photons that reach the edge light sensors and creates a curved profile when looking at the peaks of the light sensor MDRFs as a function of position.

The resolution for different depths is shown in tables with the Beer's Law weighted average for the camera shown in the last column. Each table shows the results from a single light sensor configuration for the three detector types. From this we can see that curvature does not affect the resolution in the x and y, but we do see a slight improvement in the z direction for all light sensor configurations.

5.2.2 Fibers

To determine the effects of fiber optics in a gamma-ray camera, we compared planar detectors with and without a fiber optic light guide. The total thickness of the light guide was held at 5-mm. We compared a 5-mm monolithic light guide with a combination of 2-mm monolithic and 3-mm fiber optic plate and a 5-mm fiber optic plate. The 5-mm fiber optic plate would not be as practical to build because the monolithic light guide is used to hermetically seal the scintillation crystal, but if the scintillation crystal was coated for the hermetic seal then the fiber optic plate could

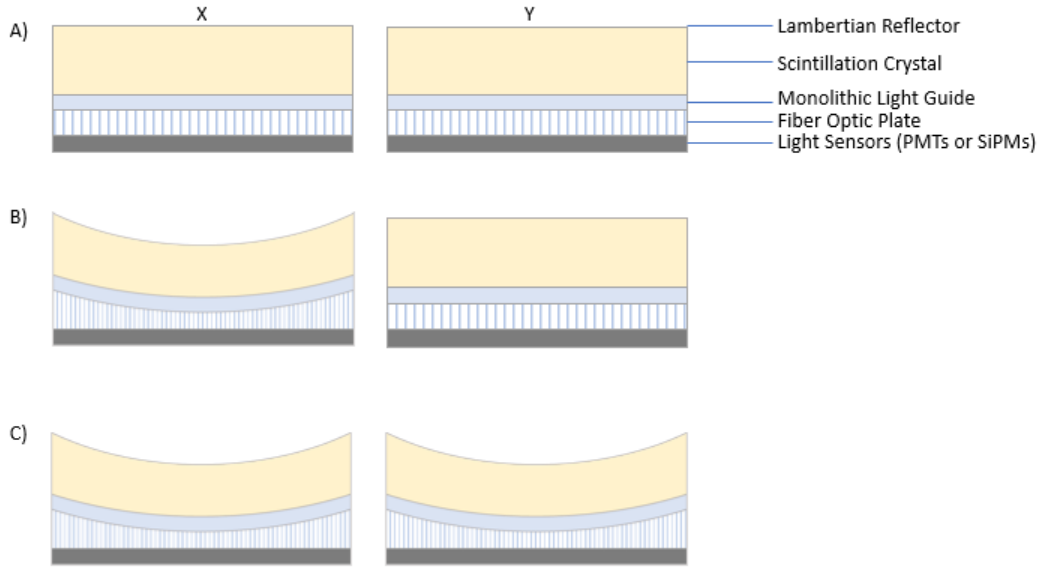

Figure 5.5: The three detectors that were tested to determine the effects of curvature on the intrinsic spatial resolution. All three included the use of fiber optics and had fiber thickness of 3-mm in the center.

be used without the use of a monolithic light guide.

From Tables 5.6, 5.7, 5.8, 5.9, we can see that by adding a fiber optic light guide there is an improvement in the x y resolution with less of a change in z resolution. From this we can conclude that the addition of fiber optics and the decrease in the spreading of the light could be advantageous to include in planar gamma-ray cameras.

Another investigation was into what percentage of photons that enter the fiber optic experience TIR down the fiber core by entering at an angle within the NA. One million photons were launched from $x = 0$, $y = 0$. The photons that experience TIR as a function of initial depth within the scintillation crystal was investigated using the planar detector that had a monolithic and fiber optic light guide. The monolithic light guide thickness was varied from 2-5 mm. Results in Table 5.10 show the percentage of photons that TIR as a function of depth and light guide thickness. Table 5.11 shows the photons that TIR as a function of curvature.

From this we can see that the initial depth did not have a large affect on the

Grid PMT Configuration

Intrinsic Spatial Resolution (mm)

Depth (mm)	1	3	5	7	Beer's Law Weighted
Planar					
x res	1.80	1.81	1.89	2.01	1.84
y res	1.87	1.86	1.92	2.03	1.89
z res	2.57	2.89	3.17	3.30	2.85
Cylindrically Curved					
x res	1.86	1.88	1.94	2.02	1.90
y res	1.73	1.78	1.84	1.93	1.79
z res	1.84	2.36	2.79	3.14	2.30
Spherically Curved					
x res	1.83	1.86	1.91	1.97	1.87
y res	1.84	1.86	1.91	1.97	1.87
z res	1.36	1.99	2.48	2.85	1.90

Table 5.2: A table of results showing the estimated intrinsic spatial resolution in x, y, and z for each depth and the Beer's Law weighted resolution for the Grid SiPM light sensor configuration. These results are in mm and shows the effects of curvature.

percentage of photons that experience TIR when entering the fiber optic plate. We did see from Table 5.11that the curvature did have a small impact at that the spherical configuration had the largest percentage of photons experiencing TIR. However, it is important to note that the spherical camera has the lowest number of photons refracting into the fiber optic plate.

5.2.3 Light Detection Configuration

As described in the simulation methods chapter, there were four light sensor configurations that were tested for each of the designs that were tested. These have been reported in the previous results, but we can see that the split SiPM configuration performs the best, followed by the grid SiPMs, split SiPMs with PMTs, and the grid of PMTs. The lowest cost is the grid of PMTs. Due to the performance and cost trade-off, the split SiPMs around the edges and corners of the camera with PMTs in

Grid SiPM Configuration

Intrinsic Spatial Resolution (mm)

Depth (mm)	1	3	5	7	Beer's Law Weighted
Planar					
x res	1.30	1.31	1.40	1.51	1.34
y res	1.37	1.35	1.42	1.53	1.39
z res	1.95	2.21	2.48	2.63	2.19
Cylindrically Curved					
x res	1.35	1.37	1.42	1.49	1.38
y res	1.26	1.29	1.35	1.43	1.30
z res	1.34	1.75	2.13	2.44	1.72
Spherically Curved					
x res	1.33	1.35	1.39	1.45	1.36
y res	1.34	1.36	1.40	1.45	1.37
z res	0.98	1.47	1.86	2.18	1.41

Table 5.3: A table of results showing the estimated intrinsic spatial resolution in x, y, and z for each depth and the Beer's Law weighted resolution for the Grid SiPM light sensor configuration. These results are in mm and shows the effects of curvature.

the center was the light sensor configuration that was chosen for AdaptiSPECT-C.

Another way of investigating the effects of the different light sensor configurations was to look at PSFs. In Figures 5.6, 5.7, 5.8, 5.9, we can see the PSF figures with the light sensor configurations overlay. The PSFs shown are for the planar camera design with both a monolithic and fiber optic light guide. From these, we can see that there is a worsening of the PSFs when directly over a light sensor, and a narrowing of the PSF when it is closer to the edge of a light sensor. This also shows that splitting the edge and corner SiPMs improves the PSF and a magnified view of this is shown in Figure 5.10 without the overlay of the light sensors. The smaller summing of the corner and edge SiPMS decreases the size of the PSF and improves the camera performance where it typically suffers the most.

Hybrid Configuration

Intrinsic Spatial Resolution (mm)

Depth (mm)	1	3	5	7	Beer's Law Weighted
Planar					
x res	1.19	1.24	1.33	1.43	1.26
y res	1.23	1.27	1.35	1.45	1.29
z res	1.65	1.90	2.05	2.11	1.84
Cylindrically Curved					
x res	1.25	1.30	1.37	1.44	1.31
y res	1.18	1.24	1.31	1.40	1.24
z res	1.31	1.65	1.89	2.05	1.59
Spherically Curved					
x res	1.22	1.28	1.35	1.42	1.28
y res	1.23	1.28	1.35	1.43	1.29
z res	1.03	1.46	1.75	1.96	1.38

Table 5.4: A table of results showing the estimated intrinsic spatial resolution in x, y, and z for each depth and the Beer's Law weighted resolution for the Hybrid light sensor configuration. These results are in mm and shows the effects of curvature.

5.3 Conclusions and Future Work

Looking at the results for curvature, there is not a change in the intrinsic spatial resolution of the gamma-ray camera from adding cylindrical or spherical curvature. The addition to curvature does increase the cost of cameras. Future work for the curvature will be using these MDRFs in a system simulation of AdaptiSPECT-C that was created by Dr. Matthew Kupinski to see the benefits of adding curvature when using a pinhole collimated system. In addition, the testing of the intrinsic spatial resolution of a curved detector will be done in the future.

When considering the addition of fiber optics to gamma-ray cameras in planar detectors, the results have shown that adding fiber optics could provide an improvement in the x and y resolution. The fiber optic plate decreases the spreading of the light in comparison to the monolithic light guide while still allowing the light to spread, thereby, improving the x,y resolution.

Split SiPM Configuration

Intrinsic Spatial Resolution (mm)

Depth (mm)	1	3	5	7	Beer's Law Weighted
Planar					
x res	1.03	1.07	1.16	1.26	1.09
y res	1.07	1.10	1.18	1.28	1.12
z res	1.51	1.75	1.91	1.98	1.70
Cylindrically Curved					
x res	1.08	1.13	1.19	1.22	1.13
y res	1.02	1.08	1.15	1.22	1.08
z res	1.17	1.49	1.73	1.91	1.44
Spherically Curved					
x res	1.06	1.11	1.17	1.24	1.11
y res	1.07	1.12	1.18	1.25	1.12
z res	0.90	1.29	1.58	1.80	1.23

Table 5.5: A table of results showing the estimated intrinsic spatial resolution in x, y, and z for each depth and the Beer's Law weighted resolution for the Split SiPM light sensor configuration. These results are in mm and shows the effects of curvature.

Using SiPMs on the edges and corners and summing the microcells into smaller light sensor areas improved the PSF and the intrinsic spatial resolution. While the full SiPM configuration performed the best, due to the cost of the SiPMs, the hybrid configuration was chosen for AdaptiSPECT-C. Using PMTs in the center decreased the cost, but keeping the SiPMs around the edges and corners kept the increase in performance when summing smaller areas which was seen in the PSF plots.

The detector design for AdaptiSPECT-C was a 183 $\times$ 183 mm flat detector with a 5 mm light guide using a hybrid light sensor readout. AdaptiSPECT-C is currently under construction as well as the modular cameras for the system. Each camera will need MDRF data and these measurements will be compared to those that were simulated in this work. At this time, it was too costly to add curvature. Cameras with curvature and fiber optics will be tested as a part of future work.

Future work also includes 3D position estimation of the gamma-rays within the

Grid PMT Configuration

Intrinsic Spatial Resolution (mm)

Depth (mm)	1	3	5	7	Beer's Law Weighted
Monolithic Light Guide					
x res	2.01	2.05	2.12	2.22	2.06
y res	2.09	2.11	2.17	2.25	2.13
z res	2.61	2.85	3.12	3.30	2.84
Monolithic and Fiber Optic Light Guide					
x res	1.80	1.81	1.89	2.01	1.84
y res	1.87	1.86	1.92	2.03	1.89
z res	2.57	2.89	3.17	3.30	2.85
Fiber Optic Light Guide					
x res	1.86	1.86	1.90	1.94	1.88
y res	1.89	1.89	1.93	1.96	1.91
z res	2.48	2.72	2.97	3.20	2.71

Table 5.6: A table of results showing the estimated intrinsic spatial resolution in x, y, and z for each depth and the Beer's Law weighted resolution for the Grid SiPM light sensor configuration. These results are in mm and shows the impact of including a fiber optic plate in planar detectors.

crystal. There are several methods available for this process include contracting grid and k-d tree. These require calibration to acquire reference data such as a 3D MDRF, therefore, the acquisition of a 3D MDRF will be necessary. Prior work on 3D MDRFs includes collecting a 2D MDRF and using a depth distribution model to create a 3D MDRF to be used with maximum likelihood (Moore et al., 2007). An alternative method created a 3D MDRF model from a measured 2D MDRF or a simulated 3D MDRF. The 3D MDRF model was found using the measured 2D or simulated 3D MDRF as a starting estimate for the model and estimating the 3D position likelihood and continuing to iterate over events until the model found steady state parameters (Hunter et al., 2009). The simulations generated by this work could be used as the 3D MDRF estimates to determing the 3D MDRF model of the cameras used for AdaptiSPECT-C. Determining the 3D MDRF for the hybrid cameras will be apart of the future work.

Grid SiPM Configuration

Intrinsic Spatial Resolution (mm)					
Depth (mm)	1	3	5	7	Beer's Law Weighted
Monolithic Light Guide					
x res	1.43	1.47	1.55	1.65	1.49
y res	1.48	1.50	1.57	1.67	1.52
z res	1.95	2.19	2.45	2.64	2.18
Monolithic and Fiber Optic Light Guide					
x res	1.30	1.31	1.40	1.51	1.34
y res	1.37	1.35	1.42	1.53	1.39
z res	1.95	2.21	2.48	2.63	2.19
Fiber Optic Light Guide					
x res	1.32	1.32	1.37	1.42	1.34
y res	1.37	1.35	1.40	1.45	1.38
z res	1.75	1.93	2.17	2.42	1.95

Table 5.7: A table of results showing the estimated intrinsic spatial resolution in x, y, and z for each depth and the Beer's Law weighted resolution for the Grid SiPM light sensor configuration. These results are in mm and shows the impact of including a fiber optic plate in planar detectors.

Hybrid Configuration

Intrinsic Spatial Resolution (mm)					
Depth (mm)	1	3	5	7	Beer's Law Weighted
Monolithic Light Guide					
x res	1.37	1.45	1.52	1.59	1.44
y res	1.39	1.47	1.54	1.61	1.46
z res	1.68	1.89	2.02	2.09	1.84
Monolithic and Fiber Optic Light Guide					
x res	1.19	1.24	1.33	1.43	1.26
y res	1.23	1.27	1.35	1.45	1.29
z res	1.65	1.90	2.05	2.11	1.84
Fiber Optic Light Guide					
x res	1.15	1.20	1.29	1.35	1.21
y res	1.17	1.23	1.31	1.37	1.23
z res	1.53	1.72	1.90	2.06	1.71

Table 5.8: A table of results showing the estimated intrinsic spatial resolution in x, y, and z for each depth and the Beer's Law weighted resolution for the Hybrid light sensor configuration. These results are in mm and shows the impact of including a fiber optic plate in planar detectors

Split SiPM Configuration

Intrinsic Spatial Resolution (mm)					
Depth (mm)	1	3	5	7	Beer's Law Weighted
Monolithic Light Guide					
x res	1.18	1.24	1.32	1.39	1.25
y res	1.20	1.26	1.33	1.41	1.26
z res	1.54	1.74	1.89	1.97	1.71
Monolithic and Fiber Optic Light Guide					
x res	1.03	1.07	1.16	1.26	1.09
y res	1.07	1.10	1.18	1.29	1.12
z res	1.51	1.75	1.91	1.98	1.70
Fiber Optic Light Guide					
x res	0.99	1.04	1.12	1.18	1.05
y res	1.01	1.06	1.14	1.20	1.07
z res	1.37	1.55	1.73	1.90	1.54

Table 5.9: A table of results showing the estimated intrinsic spatial resolution in x, y, and z for each depth and the Beer's Law weighted resolution for the Split SiPM light sensor configuration. These results are in mm and shows the impact of including a fiber optic plate in planar detectors.

Percentage of Photons that TIR				
	Intial Depth in Scintillation Crystal(mm)			
LG thickness (mm)	1	3	5	7
2	17.39	17.29	17.27	17.27
Total photons	784776	783351	780938	779372
3	17.32	17.28	17.27	17.27
Total photons	783902	781534	779459	776816
4	17.34	17.37	17.32	17.30
Total photons	783127	780627	778125	775730
5	17.37	17.33	17.35	17.35
Total photons	780432	778572	776534	774455

Table 5.10: This table shows the percentage of photons that TIR when refracting into the fiber optic plate and the total number of photons that refracted into the fiber optic plate when the gamma ray interacts at the intial position (0,0,4) as a function of light guide thickness and depth.

Percentage of Photons that TIR

	Initial Depth in Scintillation Crystal(mm)			
Curvature	1	3	5	7
Planar	17.39	17.29	17.27	17.27
Total photons	784776	783351	780938	779372
Cylindrical	16.30	16.36	16.37	16.35
Total photons	837099	817068	799952	784372
Spherical	19.14	19.19	19.31	19.55
Total photons	639004	645166	633563	608418

Table 5.11: This table shows the percentage of photons that TIR when refracting into the fiber optic plate and the total number of photons that refracted into the fiber optic plate when the gamma ray interacts at the intial position (0,0,4) as a function of curvature for a 2-mm light guide.

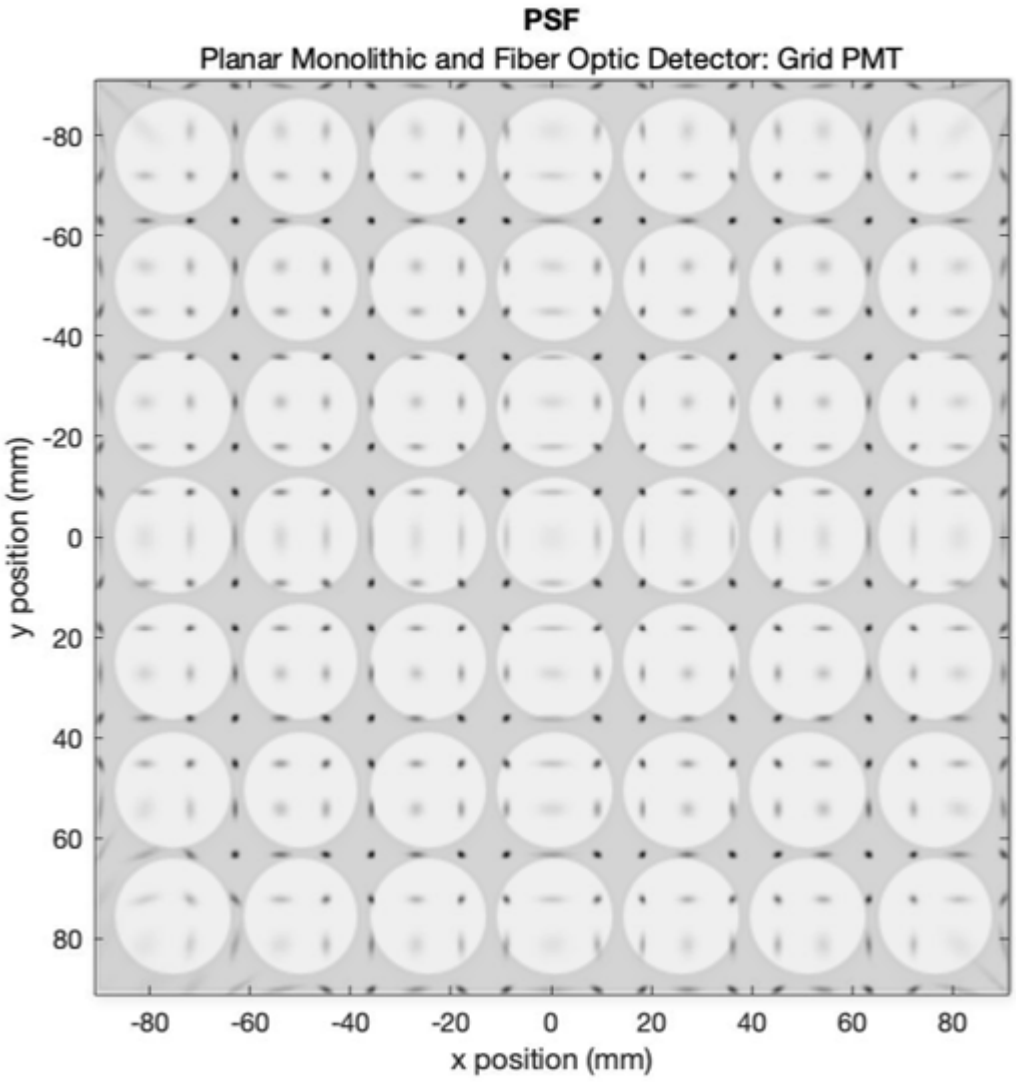

Figure 5.6: This figure shows the PSF for the planar monolithic and fiber optic light guide with the grid of PMTs for the light sensor configuration.

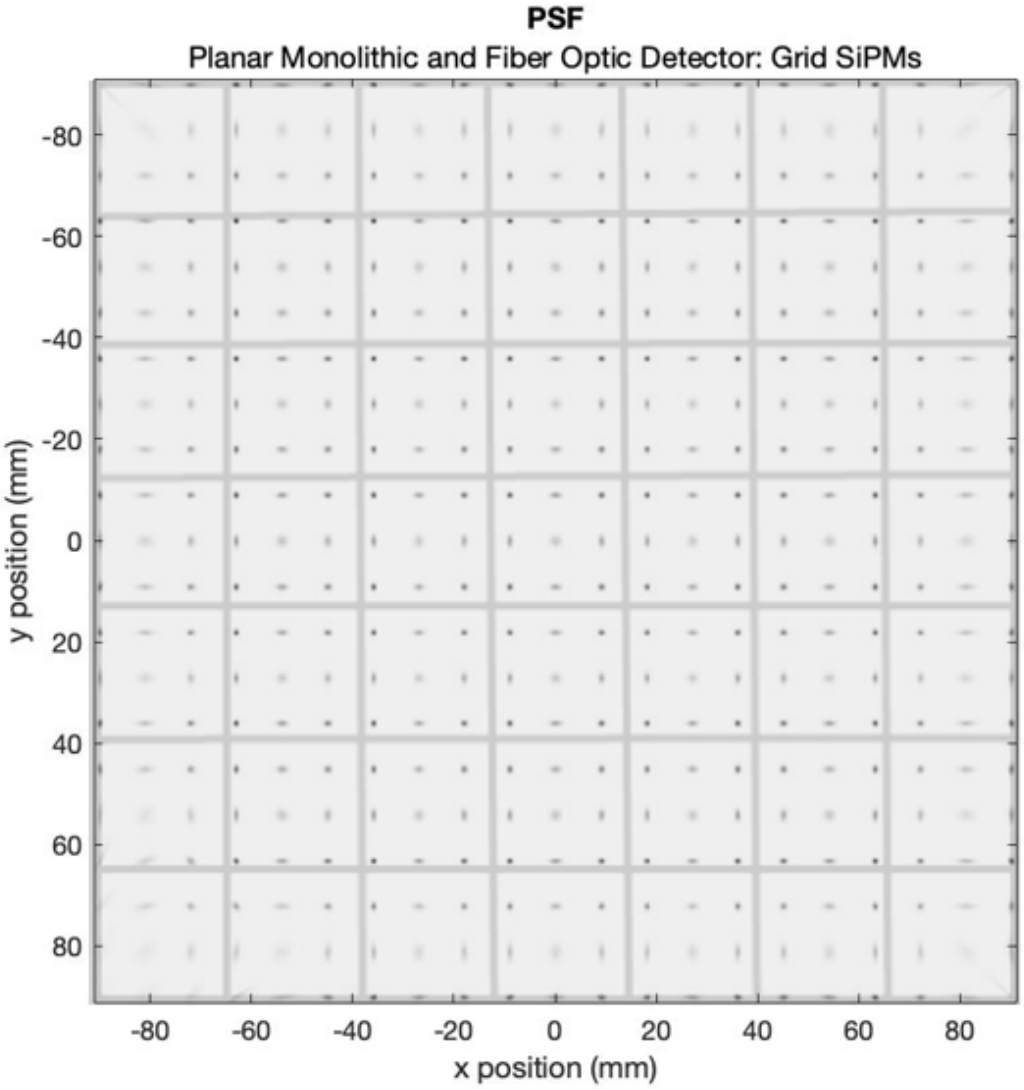

Figure 5.7: This figure shows the PSF for the planar monolithic and fiber optic light guide with the grid of SiPMs for the light sensor configuration.

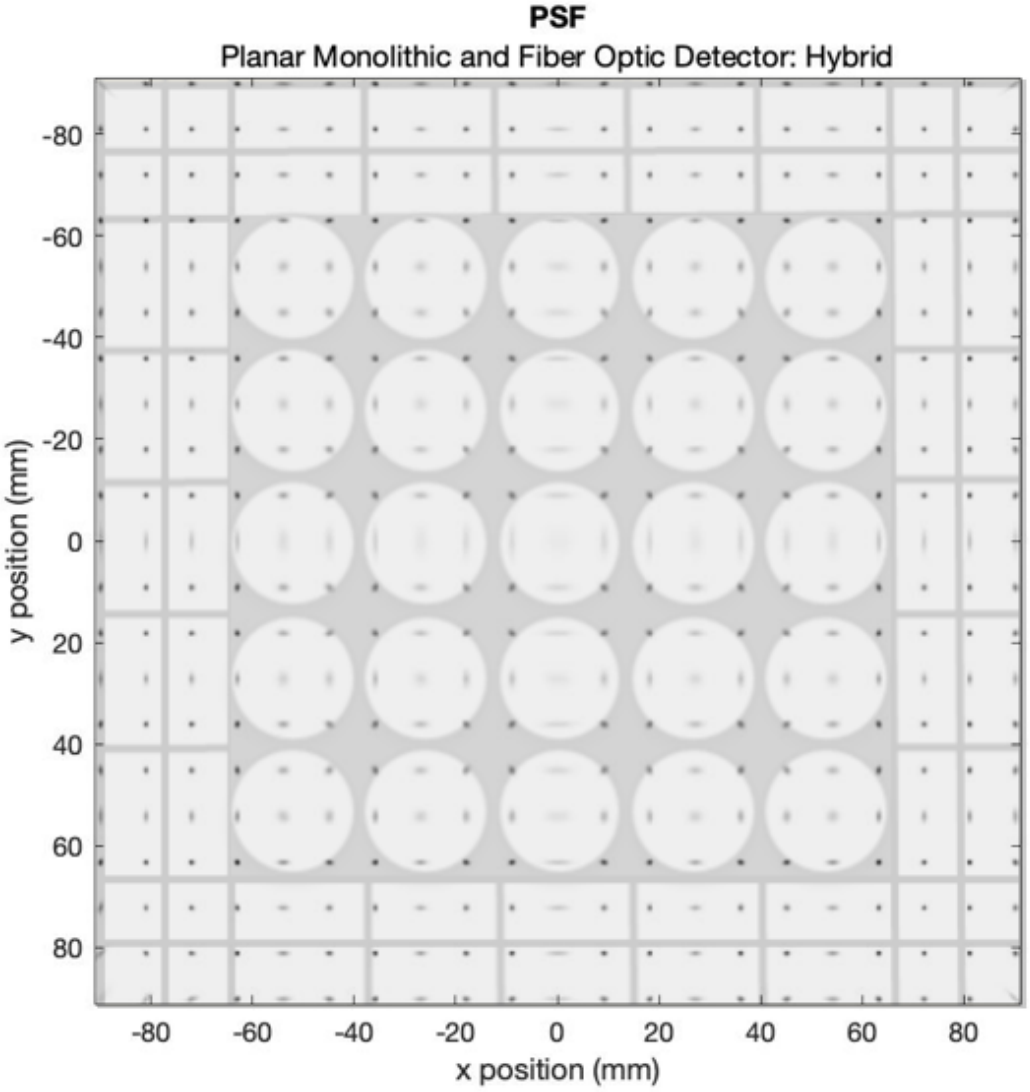

Figure 5.8: This figure shows the PSF for the planar monolithic and fiber optic light guide with the hybrid light sensor configuration.

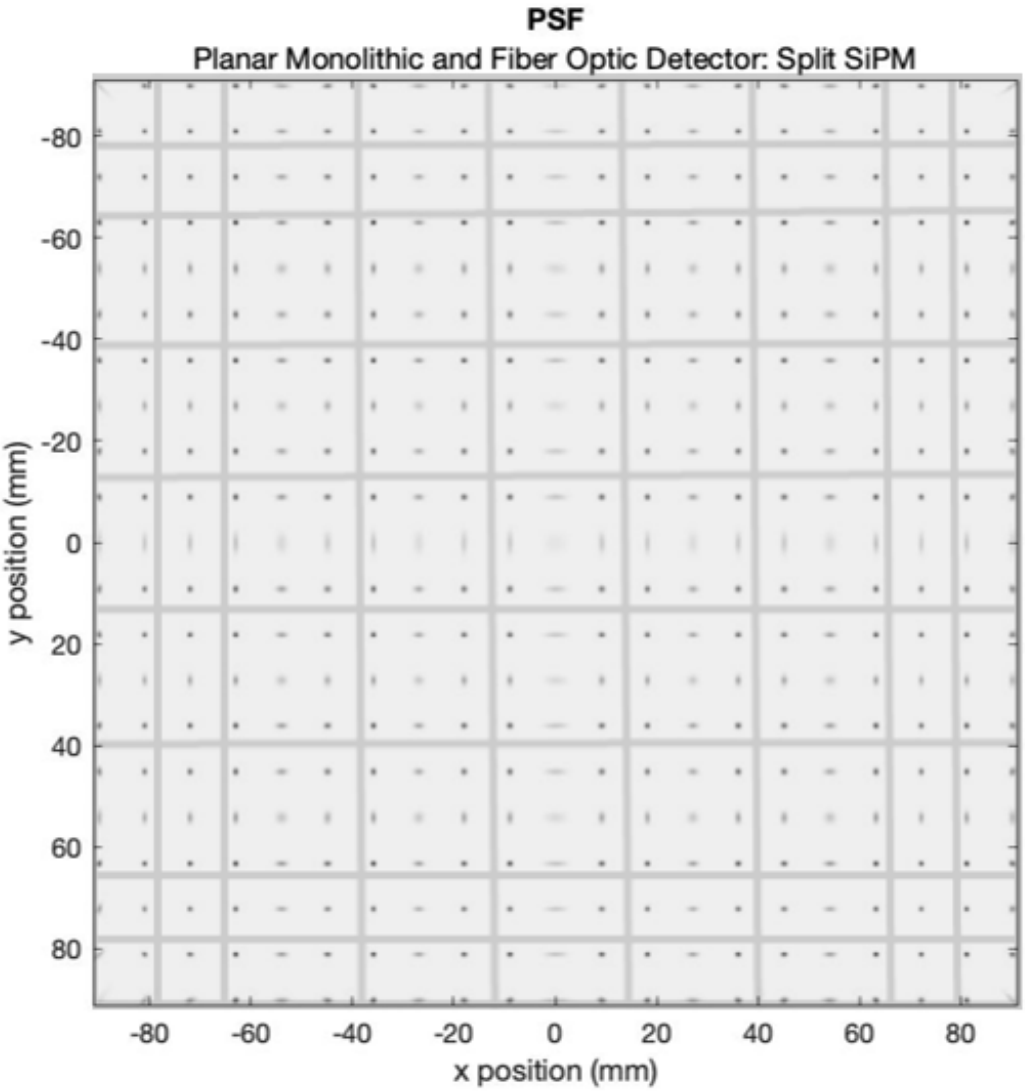

Figure 5.9: This figure shows the PSF for the planar monolithic and fiber optic light guide with the split SiPM light sensor configuration.

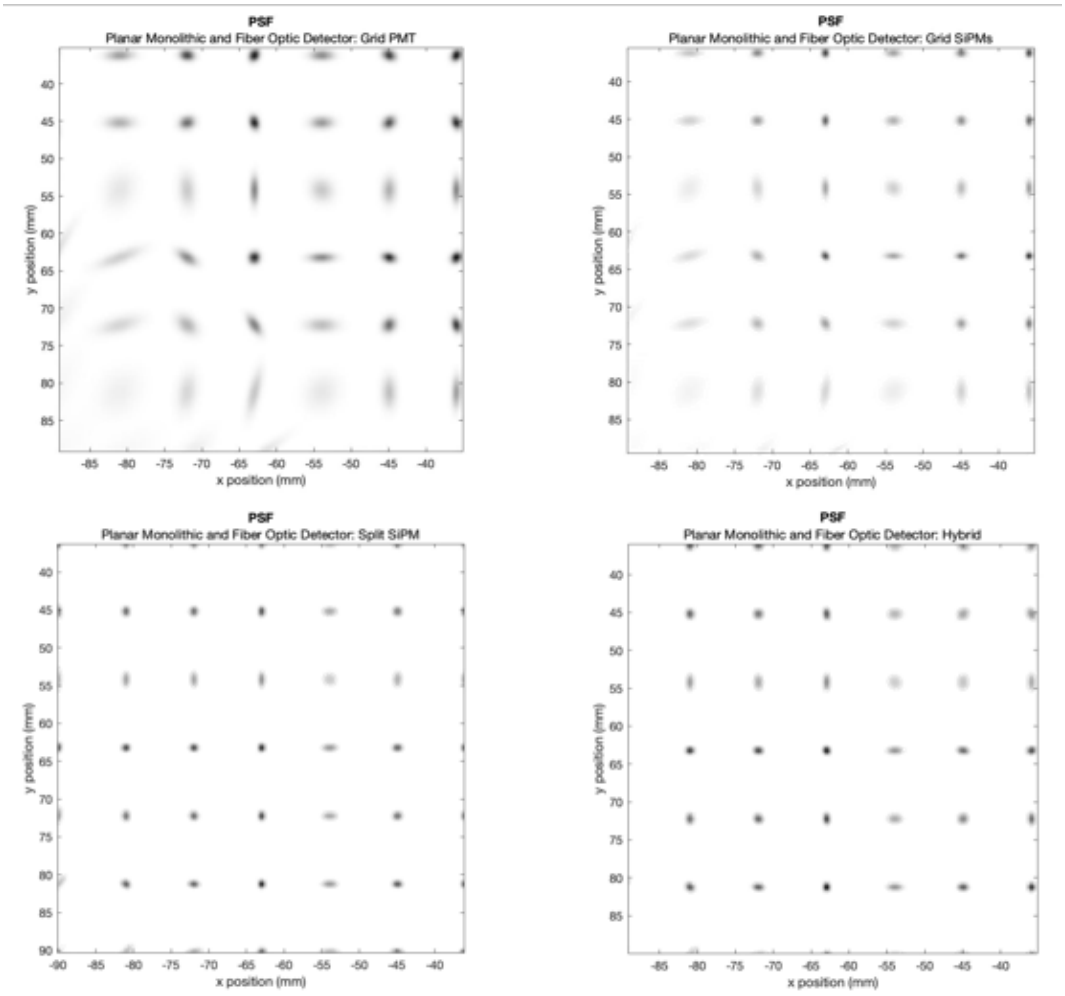

Figure 5.10: This schematic shows a larger view of the corner PSFs from the previous figures.

REFERENCES

Adam, L.-E., J. S. Karp, M. E. Daube-Witherspoon, and R. J. Smith (2001). Performance of a Whole-Body PET Scanner Using Curve-Plate NaI(Tl) Detectors. *Journal of Nuclear Medicine*, **42**(12), pp. 1821–1830. ISSN 0161-5505.

Apple Developer (2022a). Metal Software. https://developer.apple.com/metal/.

Apple Developer (2022b). Swift Software. https://developer.apple.com/swift/.

Barrett, H. H., W. C. Hunter, B. W. Miller, S. K. Moore, Y. Chen, and L. R. Furenlid (2009). Maximum-likelihood methods for processing signals from gamma-ray detectors. *IEEE Transactions on Nuclear Science*, **56**(3), pp. 725–735. ISSN 00189499. doi:10.1109/TNS.2009.2015308.

Barrett, H. H. and M. A. Kupinski (eds.) (2005). *Small-Animal SPECT Imaging*. Kluwer Academic Publishers. ISBN 038725143X.

Benadiba, M., G. Luurtsema, L. Wichert-Ana, C. A. Buchpigel, and G. B. Filho (2012). New Molecular Targets for PET and SPECT Imaging in Neurodegenerative Diseases. *Revista Brasileira de Psiquiatria*, **34**, p. 121–124. doi:10.1016/j.rbp.2012.07.002.

Bergqvist, M. (1998). A SPECT light transport simulation program. Technical report, SCAN-9910017.

Bloom, G. S. (2014). Amyloid-Pathogenesis. *JAMA Neurology*, **71**(4), pp. 505–508. ISSN 2168-6149. doi:10.1001/jamaneurol.2013.5847.

Bolognesi, M. L. (2017). Neurodegenerative drug discovery: building on the past, looking to the future. *Future Medicinal Chemistry*, **9**(8), p. 707–709. doi:10.4155/fmc-2017-0087.

Born, M. and E. Wolf (1980). *Basic Properties of the Electromagnetic Field*, p. 36–50. Pergamon Press.

Chaix, C., S. Kovalsky, M. Kosmider, H. H. Barrett, and L. R. Furenlid (2013). Integration of AdaptiSPECT: a small-animal adaptive SPECT imaging system. *Medical Applications of Radiation Detectors III*, **8853**(September 2013), p. 88530A. ISSN 0277786X. doi:10.1117/12.2029768.

Chaix, C., J. W. Moore, R. Van Holen, H. H. Barrett, and L. R. Furenlid (2012). The AdaptiSPECT imaging aperture. *IEEE Nuclear Science Symposium Conference Record*, pp. 3564–3567. ISSN 10957863. doi:10.1109/NSSMIC.2012.6551816.

Cherry, S., J. Sorenson, and M. Phelps (2012). *Physics in Nuclear Medicine E-Book*. Elsevier Health Sciences. ISBN 9781455733675.

Cronin, K. P., M. A. Kupinski, J. M. Woolfenden, G. Yabu, T. Kawamura, S. Takeda, T. Takahashi, and L. R. Furenlid (2020). Design of a Multi-Technology Pre-Clinical SPECT System. In *2020 IEEE Nuclear Science Symposium and Medical Imaging Conference (NSS/MIC)*, pp. 1–3. doi:10.1109/NSS/MIC42677.2020.9508045.

Cvijetic, M. and I. Djordjevic (2013). *Advanced optical communication systems and networks*. Artech House.

Dib, M. (2005). Issues for Clinical Drug Development in Neurodegenerative Diseases. *Drugs*, **65**(17), p. 2463–2479. doi:10.2165/00003495-200565170-00004.

Dupont, A.-C. J. S., B. J. S. Largeau, D. J. S. Guilloteau, M. J. S. Ribeiro, and N. J. S. Arlicot (2018). The Place of PET to Assess New Therapeutic Effectiveness in Neurodegenerative Diseases. *Contrast Media Molecular Imaging*, **2018**, p. 1–15. doi:10.1155/2018/7043578.

Ermis, E. E. and C. Celiktas (2015). Mass attenuation coefficient calculations of different detector crystals by means of FLUKA Monte Carlo method. In *EPJ Web of Conferences*, volume 100. ISSN 2100014X. doi:10.1051/epjconf/201510002003.

Furenlid, L. R., D. W. Wilson, Y. C. Chen, H. Kim, P. J. Pietraski, M. J. Crawford, and H. H. Barrett (2004). FastSPECT II: A second-generation high-resolution dynamic SPECT imager. *IEEE Transactions on Nuclear Science*, **51**(3 II), pp. 631–635. ISSN 00189499. doi:10.1109/TNS.2004.830975.

Georgiou, M., G. Borghi, S. V. Spirou, G. Loudos, and D. R. Schaart (2014). First performance tests of a digital photon counter (DPC) array coupled to a CsI(Tl) crystal matrix for potential use in SPECT. *Physics in Medicine and Biology*, **59**(10), pp. 2415–2430. doi:10.1088/0031-9155/59/10/2415.

Gruner, S. M., M. W. Tate, and E. F. Eikenberry (2002). Charge-coupled device area x-ray detectors. *Review of Scientific Instruments*, **73**(8), pp. 2815–2842. doi:10.1063/1.1488674.

Hamedani, G. G. and M. N. Tata (1975). On the Determination of the Bivariate Normal Distribution from Distributions of Linear Combinations of the Variables. *The American Mathematical Monthly*, **82**(9), pp. 913–915. doi:10.1080/00029890.1975.11993976.

Hunter, W. C. J., H. H. Barrett, and L. R. Furenlid (2009). Calibration Method for ML Estimation of 3D Interaction Position in a Thick Gamma-Ray Detector.

IEEE Transactions on Nuclear Science, **56**(1), pp. 189–196. doi:10.1109/TNS.2008.2010704.

Incom, M., Charlton (2022). INCOM / Enabling the Vision of Tomorrow / The Leader in Glass and Polymer Microstructures. https://incomusa.com/.

Klein, G., P. Delmar, N. Voyle, S. Rehal, C. Hofmann, D. Abi-Saab, M. Andjelkovic, S. Ristic, G. Wang, R. Bateman, and et al. (2019). Gantenerumab reduces amyloid- plaques in patients with prodromal to moderate alzheimer's disease: A pet substudy interim analysis. *Alzheimer's Research amp; Therapy*, **11**(1). doi:10.1186/s13195-019-0559-z.

Klein, W. P., H. H. Barrett, I. W. Pang, D. D. Patton, M. M. Rogulski, J. D. Sain, and W. E. Smith (1995). FASTSPECT: electrical and mechanical design of a high-resolution dynamic SPECT imager. *IEEE Nuclear Science Symposium Medical Imaging Conference*, **2**, pp. 931–933. doi:10.1109/nssmic.1995.510420.

Korevaar, M. A. N., J. W. T. Heemskerk, and F. J. Beekman (2009). A pinhole gamma camera with optical depth-of-interaction elimination. *Physics in Medicine Biology*, **54**(13), p. N267. doi:10.1088/0031-9155/54/13/N02.

Li, X., L. Tao, C. S. Levin, and L. R. Furenlid (2019). Fast gamma-ray interaction-position estimation using k-d tree search. *Physics in Medicine and Biology*, **64**(15). ISSN 13616560. doi:10.1088/1361-6560/ab0da6.

May, M., N. C. Momsen, R. G. Richards, K. S. Kalluri, N. Zeraatkar, B. Auer, M. A. King, P. H. Kuo, and L. R. Furenlid (2020). Design of Adaptive Pinhole SPECT Collimators for Improved Spatial Resolution and Sensitivity. *2020 IEEE Nuclear Science Symposium and Medical Imaging Conference, NSS/MIC 2020*, pp. 2020–2022. doi:10.1109/NSS/MIC42677.2020.9508064.

Meng, L. (2006). An Intensified EMCCD Camera for Low Energy Gamma Ray Imaging Applications. *IEEE Transactions on Nuclear Science*, **53**(4), pp. 2376–2384. doi:10.1109/TNS.2006.878574.

Miller, B. W., L. R. Furenlid, S. K. Moore, H. B. Barber, V. V. Nagarkar, and H. H. Barrett (2009). System integration of FastSPECT III, a dedicated SPECT rodent-brain imager based on BazookaSpect detector technology. *IEEE Nuclear Science Symposium Conference Record*, pp. 4004–4008. ISSN 10957863. doi:10.1109/NSSMIC.2009.5401924.

Milster, T. D., J. N. Aarsvold, H. H. Barrett, A. Landesman, L. Mar, D. D. Patton, T. J. Roney, R. K. Rowe, and R. H. Seacat III (1990). A full-field modular gamma camera. *Journal of Nuclear Medicine*, **31**(5), pp. 632–639. ISSN 01615505.

Moore, S., W. Hunter, L. Furenlid, and H. Barrett (2007). Maximum-likelihood estimation of 3D event position in monolithic scintillation crystals: Experimental results. **5**, pp. 3691–3694. doi:10.1109/NSSMIC.2007.4436923.

Myers, W. G. and H. N. Wagner (1974). Nuclear Medicine: How It Began. *Hospital Practice*, **9**(3), pp. 103–113. doi:10.1080/21548331.1974.11707967.

Ostrowitzki, S., R. A. Lasser, E. Dorflinger, P. Scheltens, F. Barkhof, T. Nikolcheva, E. Ashford, S. Retout, C. Hofmann, and P. Delmar (2017). A phase III randomized trial of gantenerumab in prodromal alzheimer's disease. *Alzheimer's Research amp; Therapy*, **9**(1). doi:10.1186/s13195-017-0318-y.

Peterson, T. E. and L. R. Furenlid (2011). SPECT detectors: The Anger Camera and Beyond. *Physics in Medicine and Biology*, **56**(17).

Photonics, H. (2022). Hamamatsu Photonics.

Piemonte, C. and A. Gola (2019). Overview on the main parameters and technology of modern Silicon Photomultipliers. *Nuclear Instruments and Methods in Physics Research, Section A: Accelerators, Spectrometers, Detectors and Associated Equipment*, **926**(August 2018), pp. 2–15. ISSN 01689002. doi: 10.1016/j.nima.2018.11.119.

Prince, J. L. and J. M. Links (2006). *Medical imaging: signals and systems*. Pearson Education.

Richards, R. G., M. Ruiz-Gonzalez, M. May, K. J. Doty, K. S. Kalluri, N. Zeraatkar, B. Auer, M. A. King, P. H. Kuo, and L. R. Furenlid (2020). Hardware Development of Hybrid-Sensor Cameras and Gantry for an Adaptive SPECT System. *2020 IEEE Nuclear Science Symposium and Medical Imaging Conference, NSS/MIC 2020*, pp. 2020–2022. doi:10.1109/NSS/MIC42677.2020.9508102.

Rogulski, M. M., H. B. Barber, H. H. Barrett, R. L. Shoemaker, and J. M. Woolfenden (1993). Ultra-high-resolution brain spect imaging: Simulation results. *IEEE Transactions on Nuclear Science*, **40**(4), pp. 1123–1129. ISSN 15581578. doi:10.1109/23.256722.

Rossmann, K. (1969). Point Spread-Function, Line Spread-Function, and Modulation Transfer Function. *Radiology*, **93**(2), pp. 257–272. doi:10.1148/93.2.257. PMID: 5822701.

Saint-Gobain Crystals (2020). NaI(Tl) and Polyscin® NaI(Tl) Sodium Iodide Scintillation Material Datasheet.

Saveliev, V. (2004). The recent development and study of silicon photomultiplier. In *Nuclear Instruments and Methods in Physics Research, Section A: Accelerators, Spectrometers, Detectors and Associated Equipment*, volume 535, pp. 528–532. ISSN 01689002. doi:10.1016/S0168-9002(04)01721-8.

Shi, M., F. Chu, F. Zhu, and J. Zhu (2022). Impact of Anti-amyloid-β Monoclonal Antibodies on the Pathology and Clinical Profile of Alzheimers Disease: A Focus on Aducanumab and Lecanemab. *Frontiers in aging neuroscience*, **14**. doi:10.3389.

Swanson, C., Y. Zhang, S. Dhadda, J. Wang, J. Kaplow, R. Lai, L. Lannfelt, H. Bradley, M. Rabe, A. Koyama, L. Reyderman, D. Berry, S. Berry, R. Gordon, L. Kramer, and J. Cummings (2021). A randomized, double-blind, phase 2b proof-of-concept clinical trial in early Alzheimer's disease with lecanemab, an anti-A protofibril antibody. *Alzheimers Res Ther.*, **13**. doi:10.1186/s13195-021-00813-8.

Tate, M. W., S. M. Gruner, and E. F. Eikenberry (1997). Coupling format variations in x-ray detectors based on charge coupled devices. *Review of Scientific Instruments*, **68**(1), pp. 47–54. doi:10.1063/1.1147611.

Wernick, M. and J. Aarsvold (eds.) (2004). *Emission tomography: the fundamentals of PET and SPECT*. Academic Press.